frontiers | Frontiers in Earth Science

TYPE Original Research
PUBLISHED 28 March 2025
DOI 10.3389/feart.2025.1568199

OPEN ACCESS

EDITED BY
Dicky Harishidayat,
Pertamina Hulu Energi, Indonesia

REVIEWED BY
Zuochun Fan,
China University of Geosciences
Wuhan, China
Raed Badr,
Cairo University, Egypt

*CORRESPONDENCE
Dou Luxing,
douluxing@hotmail.com

RECEIVED 29 January 2025
ACCEPTED 10 March 2025
PUBLISHED 28 March 2025

CITATION
Xiaoyang G, Luxing D, Wenxiang H, Qi S, Zhenli Y, Bin L, Qiaolin H, Jineng J, Yong H, Jingwen Y and Li Z (2025) The control of small-scale syndepositional normal faults on sandstone distribution: example from the Paleogene bottom Sandstone Member in the Tabei Uplift, Tarim Basin, China.
Front. Earth Sci. 13:1568199.
doi: 10.3389/feart.2025.1568199

The control of small-scale syndepositional normal faults on sandstone distribution: example from the Paleogene bottom Sandstone Member in the Tabei Uplift, Tarim Basin, China

Gao Xiaoyang[1], Dou Luxing[1]*, He Wenxiang[1], Sun Qi[2], Yi Zhenli[2], Li Bin[2], He Qiaolin[2], Jin Jineng[3], Hu Yong[1], Yan Jingwen[2] and Zhang Li[3]

[1]College of Resources and Environment, Yangtze University, Wuhan, China, [2]Research Institute of Exploration and Development, Tarim Oilfield Company, CNPC, Korla, China, [3]School of Geosciences, Yangtze University, Wuhan, China

Introduction: The syndepositional normal faults related paleogeomorphic units in sedimentary basins play a crucial role in controlling sediment transport and infill processes. Previous studies have primarily focused on the control of depositional systems by large-scale syndepositional faults. However, there is still a lack of systematic understanding about the control of intensively developed small-scale syndepositional normal faults on sandstone facies distribution in continental basin.

Methods: This study integrates 3D seismic data, well logs, and core descriptions to determine the depositional facies and small-scale syndepositional normal fault related paleogeomorphology are consistent during deposition of the Paleogene Bottom Sandstone Member of the WM7 fault zone area in the Tabei Uplift, Tarim basin.

Results: The results indicate that the Paleogene Bottom Sandstone Member consists of deltaic sandstone facies and fine-grained lacustrine deposits containing evaporites near an erosional uplift. During the deposition of the Bottom Sandstone Member, an erosional uplift zone developed in the eastern part of the WM7 fault zone, where numerous incised valleys formed. In contrast, the fault zone and its western region were characterized by a delta–saline lake depositional system controlled by a syndepositional graben, with numerous small-scale en echelon syndepositional faults developing within the fault zone.

Discussion: These special geomorphic units composed of syndepositional faults were primarily formed by differential subsidence of strata. These faults and their associated paleogeomorphic units controlled the distribution characteristics of incised valleys and distributary channels. By analyzing the control exerted by micro - geomorphic units composed of syndepositional normal faults near the paleo-uplift on the distribution of sandstone, new insights are provided for

predicting the distribution of sandstone in complex geomorphic units formed by small-scale syndepositional fault combinations in continental basins.

KEYWORDS

seismic sedimentology, sandstone distribution, syndepositional fault, salt lake-delta, tabei uplift, paleogene

1 Introduction

The sedimentary processes of terrestrial basins are strongly influenced by tectonic activity and climate change, with diverse controlling factors and rapid facies changes. This has resulted in limited understanding of clastic material erosion, transportation, and deposition processes, making sand body prediction challenging. Current research on sand-controlling mechanisms in terrestrial basins focuses on geomorphological, sequence stratigraphic, and climatic controls (Xu, 2013; Shi et al., 2017; Mulrooney et al., 2018; Liu et al., 2019; Nie et al., 2022). Among these, paleogeomorphology, as the surface morphology during geological history, determines sediment transport pathways and depositional sites (Normark, 1970). Extensive research has demonstrated that paleogeomorphology primarily influences sedimentary types and distribution patterns. The paleogeomorphological setting controls sedimentary system types, while specific geomorphic units govern the distribution of sedimentary sand bodies (Hou et al., 2018; Dong et al., 2016; Liu et al., 2019; Yang Z. et al., 2023).

Current research on geomorphological sand-controlling mechanisms primarily focuses on two aspects: sand control by incised valleys and sand control by slope breaks (Dong et al., 2016; Dou et al., 2020a; Cao et al., 2022). Among these, paleovalleys are residual accommodation spaces formed by erosion when the base level falls below the slope break zone. They represent direct evidence of sediment transport, serving both as conduits for delivering sediments from source areas to basins and as indicators of fluvial flow directions, controlling the preferential direction of sand body accumulation (Feng, 2006; Dong et al., 2016; Tian et al., 2019). As early as the study of submarine fans, a strong correspondence between valleys and fan bodies was identified (Walker, 1978). Through research on valley types, characteristics, and their control on sedimentary facies development, significant success has been achieved in predicting the distribution and scale of sand bodies as well as in the exploration of hydrocarbon reservoirs (Xu et al., 2004; Xu, 2013; Feng, 2006). The slope break zone represents a transitional area in depositional geomorphology, where changes in stratal dip induce variations in sedimentary dynamics. This zone significantly influences the accommodation space and depositional processes within the basin, constraining the spatial distribution of sedimentary facies (Shu et al., 2013; Cao et al., 2022). Slope break zones generated by syndepositional fault activity under tectonic subsidence are a common geomorphological feature. Numerous studies have focused on the role of large-scale syndepositional faults in sand body Formation, analyzing the control mechanisms of various fault combination styles and slope gradients on sand body morphology and distribution patterns (Lin et al., 2000; Zhou et al., 2014; Chen et al., 2014). However, during basin subsidence, dense small-scale syndepositional faults often develop, resulting in complex micro-paleogeomorphological units. These units exert significant control over the distribution of clastic sedimentary facies in localized areas, providing critical details for reservoir prediction and oilfield development planning in key hydrocarbon-bearing intervals (Mulrooney et al., 2018; Dou et al., 2020a; Dou et al., 2020b). At present, research on the control of small-scale geomorphological units formed by minor syndepositional faults on depositional filling remains insufficiently explored. This has resulted in numerous small-scale syndepositional faults being incorrectly identified, thus hindering an accurate understanding of the depositional processes in regions where such faults developed.

The Tarim Basin is a large superimposed basin that transitioned into a rift-depression phase during the Late Cretaceous-Paleogene, accumulating substantial sedimentary infill (Ding et al., 1996; Wu G. et al., 2020). During this period, the northern Tarim Basin experienced complex tectonic movements and was in a phase of tectonic subsidence (Zhao et al., 2012; Wu G. et al., 2020). As a result, numerous syndepositional faults developed in the Tabei Uplift under an extensional tectonic regime (Jia, 1997; He et al., 2001; Wei et al., 2001). In particular, small-scale syndepositional normal faults assemblages were formed near the slope-break zones of the ancient uplift during the deposition of the Bottom Sandstone Member of the Paleogene in the Yingmaili structural belt. These fault assemblages provide favorable conditions for studying sand-controlling mechanisms associated with small-scale syndepositional faults. This study first utilized core and well log data to determine the depositional environment of the Bottom Sandstone Member of the Paleogene in the WM7 fault zone. Subsequently, syndepositional faults in the WM7 fault zone were identified using 3D seismic data. Through seismic horizon interpretation, the geomorphological development characteristics were clarified, and the distribution patterns of sedimentary facies were analyzed using seismic attributes and sand body thickness. Additionally, based on the interpretation of faults near the ancient uplift from seismic profiles, this study analyzed the Formation mechanisms of syndepositional faults in the context of tectonic evolution. Finally, based on the characteristics of syndepositional faults and sand body distribution, the control of different fault assemblage patterns on sand deposition was analyzed, and a syndepositional fault–graben–slope sand-controlling model was established.

2 Geological setting

The Tarim Basin, located in the southern part of Xinjiang Uyghur Autonomous Region in northwest China, is the largest inland basin in the country (Wang et al., 2024). The Tarim Basin is located amidst the Tianshan Mountains, Kunlun Mountains, and Altun Mountains (Figure 1A). It extends up to 520 km in width from north to south and 1,400 km in length from east to west, encompassing an area of approximately 560,000 km^2. The basin's

altitude varies between 800 and 1,300 m, with a general slope descending from west to east. The Tarim Basin is a large, composite basin formed by the superposition of the Paleozoic marine cratonic basin and the Mesozoic-Cenozoic foreland basin. It is subdivided into seven first-order tectonic units and 32 second-order tectonic units. The cratonic region (platform area) of the basin consists of the Tabei Uplift, North Depression, Southeast Uplift, and Central Uplift, while the foreland basin area includes the Kuqa Depression, Southwest Depression, and Southeast Depression (Huang et al., 2018). The Tabei Uplift, located in the northern part of the Tarim Basin (Figure 1B), is bordered by the Kuqa Depression to the north and the North Depression to the south. It extends approximately 480 km in an east-west direction and spans 70–100 km from north to south (An et al., 2009). Compared to the neighboring depression areas, the Tabei Uplift is characterized by significant multi-phase unconformities, significant uplift and erosion, and complex faulting. It has experienced intense tectonic activity (Figure 1D) (Wu et al., 2009). The study area is located within the WM7 fault zone in the western part of the Tabei Uplift, which is a third tectonic belt trending northeast-southwest (Figure 1C). During the Cretaceous to Paleogene period, tectonic activity in the western Tabei Uplift entered a phase of stability, characterized by stress relaxation and sedimentary subsidence. The WM7 fault zone developed a series of northeast-trending normal faults associated with the Yanshan-Himalayan orogeny (He et al., 2001). These faults gave rise to numerous Paleogene to Cretaceous faulted anticlines, faulted noses, and fault blocks (Wu et al., 2014).

The Paleogene strata in the WM7 fault zone of the study area consist of the Suweiyi Formation and the Kumugeliemu Group. The Kumugeliemu Group is composed, from bottom to top, of the Bottom Sandstone Member, Lower Gypsum Mudstone Member, Gypsum Mudstone Member, and Upper Gypsum Mudstone Member. Among them, the Bottom Sandstone Member is angularly unconformable with the underlying Bashijiqike Formation. The Bashijiqike Formation is mainly a set of brownish-red medium- to fine-grained sandstones, predominantly deposited in a braided river system (Zhang et al., 2021). A set of grayish-white fine-grained sandstones develops at the top, which is called the White Sandstone Member and is angularly unconformable with the overlying Paleogene strata (He et al., 2024). In the Tabei Uplift, the Bottom Sandstone Member mainly develops a sedimentary system of salt lake-delta (Zhao et al., 2014; Wu G. et al., 2020). According to the lithological changes, this Member can be divided into the lowstand systems tract (LST), transgressive systems tract (TST), and highstand systems tract (HST) from bottom to top (Figure 2A). The LST is mainly composed of sandstones, representing a deltaic sedimentary environment (Wu J. et al., 2020); the TST is characterized by mudstones, which are stably distributed throughout the area, reflecting saline lake deposition (Chen et al., 2017); the HST is mainly composed of grayish-white gypsum and has a wide distribution range (Chen et al., 2017), indicating a sedimentary environment in which the lake basin contracted and the salinity increased under arid climatic conditions, resulting in a gradual decline of the lake level. This study mainly focuses on the LST of the Bottom Sandstone Member of the Paleogene in the WM7 fault zone, which is characterized by a set of grayish-white fine-grained sandstones (Figure 2A).

3 Dataset and methodology

In this study, the WM7 fault zone is covered by post-stack 3D seismic data, spanning an area of approximately 9,000 km^2 (Figure 1C). The effective frequency range is 8–40 Hz, with a dominant frequency of approximately 27 Hz. The seismic wave peak represents positive polarity and is minimum phase. The vertical resolution is 41.5 m. Additionally, to precisely analyze the main controlling factors of sand bodies, a high-quality 3D seismic dataset was employed to study their distribution patterns. This dataset, covering an area of about 400 km^2 (highlighted by the blue box in Figure 1C), has an effective frequency range of 5–70 Hz, a dominant frequency of approximately 51 Hz, a seismic wave peak representing positive polarity, a minimum phase, and a vertical resolution of 22.6 m. This study examined approximately 65 m of core, which was subjected to detailed description and photographic documentation. Additionally, well logs and mud logging data from 60 wells were collected to identify lithology and depositional facies in non-cored wells.

In this study, synthetic seismograms were generated and well-to-seismic ties were conducted (Figures 2B, C) based on acoustic transit-time (AC) and density (DEN) logs. The well-to-seismic correlation in the study area is well-aligned. On this basis, 3D seismic data in the study area were interpreted. The basal boundary of the Paleogene is characterized in the seismic data by a set of high-amplitude red (trough) seismic reflections (Figures 2B, C, line E_b), which is consistent with previous studies (Zhang et al., 2021). The top boundary of the Bottom Sandstone Member, the base of the White Sandstone Member, and the base of the Gypsum Mudstone Member are all marked by strong black (peak) seismic reflections, which exhibit good continuity and can be traced across the entire study area.

To analyze the control mechanisms of graben areas in the slope zone and small-scale syndepositional faults within these graben areas on sand bodies, this paper identified 13 types of lithofacies (Table 1) based on core observations, and combined with logging curves to discriminate the sedimentary facies. The identification of syndepositional faults is primarily based on the seismic reflection characteristics from 3D seismic data, and fault interpretation is used to analyze the fault's profile and planar distribution patterns. During seismic stratigraphic interpretation, a large number of incised valley reflections were identified near the base of the Paleogene in the eastern section of the WM7 fault zone. These incised valleys show a certain correspondence with the clastic sedimentary bodies (Normark and Valleys, 1978). This study provides a detailed characterization of valleys using seismic reflections and analyzes their geomorphological development features in conjunction with the interpretation of seismic horizons. Additionally, based on fine well-seismic calibration, the maximum amplitude attribute was extracted along isochronous stratigraphic interfaces. By combining these with the valley development patterns, the distribution characteristics of sand bodies were comprehensively analyzed. Finally, by analyzing the fault development characteristics of the WM7 fault zone in the pre-Cretaceous sedimentary period to the Paleogene, and combining with the tectonic evolution background, the origin of the graben on the slope break and the small-scale syndepositional faults within

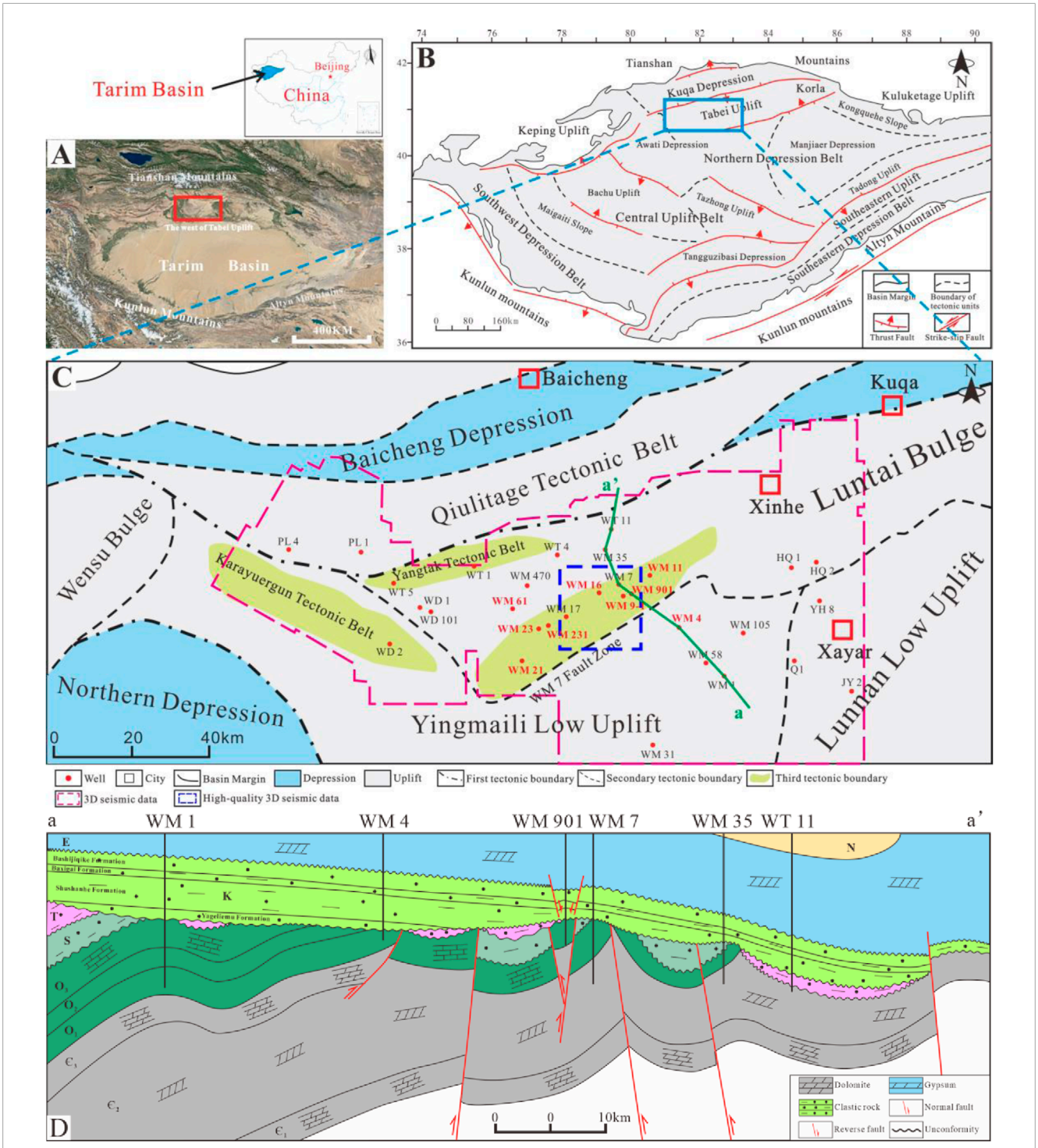

FIGURE 1
Location map of the study area **(A)** Satellite image of the Tarim Basin, with the study area located in the northern Tarim Basin **(B)** Tectonic unit division of the Tarim Basin, with the study area located in the western Tabei Uplift **(C)** Tectonic unit division of the western Tabei Uplift, with the study area located in the WM7 fault zone **(D)** The structural profile of the study area in the SE-NW direction. The location of the profile is shown in **[(C) (a~a')]**. This figure is sourced from the internal materials of Tarim Oilfield.

it, which represent a special geomorphology, was explored. A comparison is made between the distribution characteristics of sand bodies and sedimentary facies and their relationship with the palaeogeography, in order to analyze the control of these unique landforms on sand bodies and establish a sand body control model.

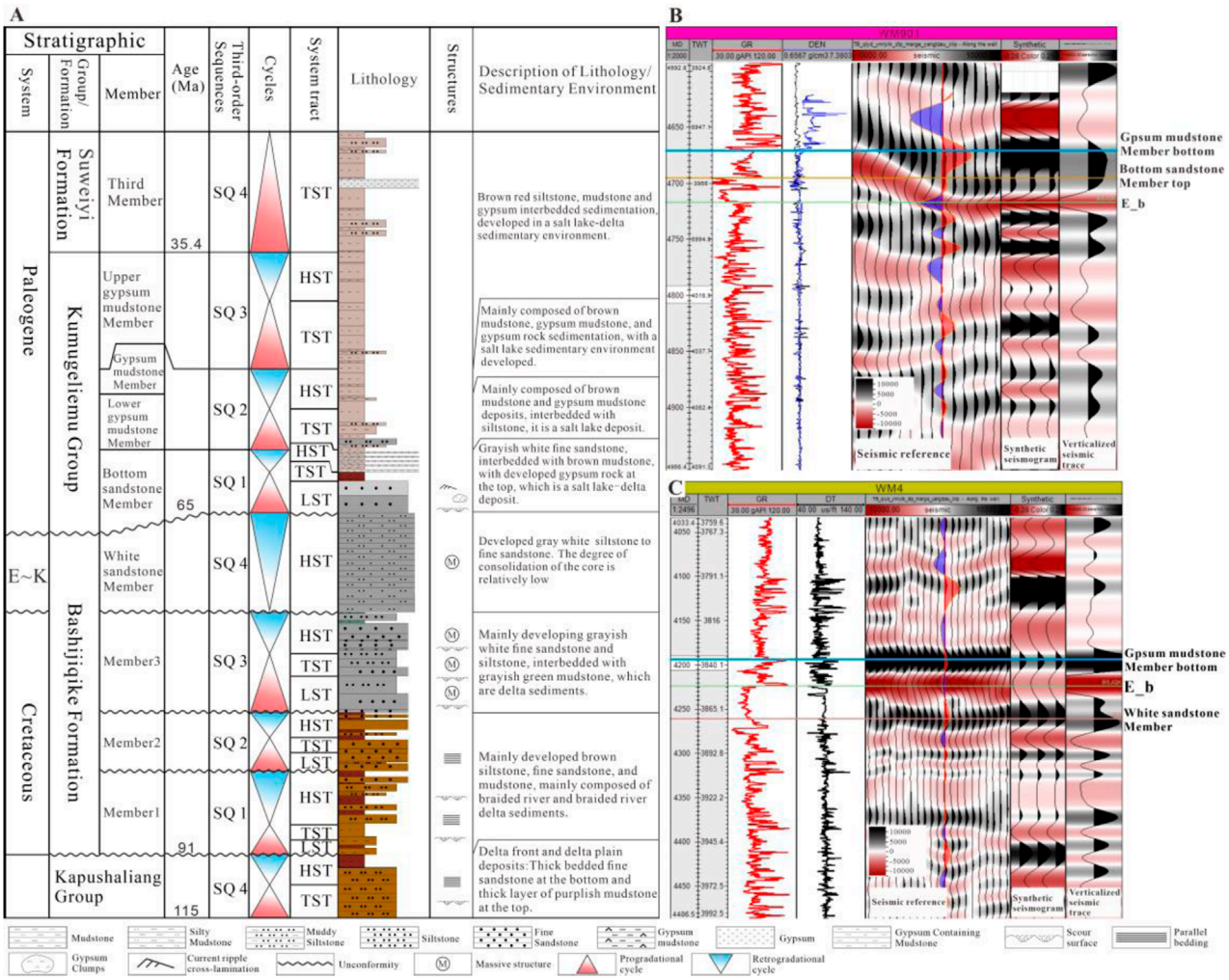

FIGURE 2
Note: E~K, End of the Cretaceous to the Paleogene; E_b, The bottom boundary of the Paleogene. Stratigraphic development characteristics of the WM7 fault zone **(A)** modified after Zhang et al. (2021) and synthetic seismic records of the target formation in typical wells **(B)** Well-to-seismic tie for wellbore WM901, where the white sandstone interval is absent **(C)** Well-to-seismic tie for wellbore YM4, where the basal sandstone interval is absent. The drilling locations of wellbores WM901 and WM4 are shown in Figure 1C in red text.

4 Results

4.1 Sedimentary facies description and interpretation of the WM7 fault zone

Based on core observations and well log curves, sedimentary facies in the WM7 fault zone can be identified. The study area is divided into five sedimentary facies associations (FA1–FA5) based on lithology, sedimentary structures, and vertical sequences. Well log characteristics are then compared with core data to identify sedimentary facies across all wells. An overview of the description and interpretation of the sedimentary facies is provided below.

4.1.1 Delta

4.1.1.1 Distributary channel (FA1)

4.1.1.1.1 Description FA1 is mainly composed of grayish-white fine-grained sandstone, with massive structures predominant (Figure 3C). Vertically, multiple progradational sand bodies are observed, but with minimal grain size variation. The bottom often shows scour surfaces with gray-green mudstone clasts and white gypsum clumps (Figures 3A, D, E), in abrupt contact with the underlying mudstone. Upward, parallel bedding is observed (Figure 3B). The lithofacies of FA1 are mainly composed of Se, Sm, and Sp. The GR (Gamma Ray) log curve for FA1 exhibits a box-shaped pattern.

4.1.1.1.2 Interpretation. FA1 is interpreted as a distributary channel deposit (Yang T. et al., 2023). Both massive structures (Sm) and parallel bedding (Sp) are characteristic of high-energy hydrodynamic environments (Miall, 1996). In particular, under relatively arid climatic conditions, seasonal river channels and extreme flood events are common, resulting in high river discharge and the Formation of high-concentration flows. These conditions favor the development of strong hydrodynamic sedimentary

TABLE 1 Lithofacies Classification and Interpretation of the Bottom Sandstone Member of the WM7 Fault Zone [The facies codes are modified according to Miall (1996)].

Code	Lithology	Sedimentary structure	Sedimentary interpretation
Mm1	Grayish-green mudstone	Irregular gypsum clumps are commonly seen. Gypsum can fill in the fractures, and there is a distinct boundary between the gypsum and the mudstone.	Mainly formed in the early diagenetic stage. Under the condition of pore water with high salinity, gypsum crystallizes and grows into clumps in the pores and micro-fractures of the mudstone (Luo et al., 2019; Wei et al., 2022).
MG	Grayish-green gypsum-rich mudstone	Gypsum and mudstone are mixed and deposited, and there is no obvious boundary line between the mudstone and the gypsum.	Formed in an environment with relatively weak hydrodynamic force. Fine-grained materials input from the land source can be deposited relatively stable at the bottom of the saline lake. At the same time, with the evaporation of the saline lake, these materials are deposited together with gypsum to form gypsum mudstone (Wang et al., 2020).
Mm2	Grayish-green mudstone	Massive structure	A stable and low-energy reducing environment (Deng et al., 2025)
Gm	White Gypsum	Massive structure	In a stable salt lake environment, there is a lack of clastic material input (Liu et al., 2023).
Ml	Grayish-green mudstone, Muddy siltstone	Lenticular bedding	Alternating hydrodynamics with influence of wave action (Zhao et al., 2015).
DMm	Grayish-green dolomitic mudstone	Massive structure, with occasional mud clasts	Formed in an environment with relatively high salinity and low hydrodynamic energy. The presence of mud clasts may indicate a flood event (Benison and Goldstein, 2001).
Sm	Grayish white siltstone/fine sandstone	Massive structure	In the upper flow regime, sediments undergo rapid deposition (Brian and Brian, 1983).
Se	Gray fine sandstone	Erosional base; lag deposit, Rip up mud clast, muddy clasts or gypsum lumps	During flood events, mudstone or gypsum deposits undergo reworking, transforming into lag deposits at the base of the distributary channels (Alonso-Zarza et al., 2009).
Sp	Grey-green fine sandstone	Parallel bedding	Deposit during flood period in upper flow regime (Zhang et al., 2018a).
Svtf	Gray-white very fine sandstone	Flame structures	During the rapid sedimentation process, the sediments are subjected to the compaction of new sediments before they are fully consolidated (Taşgın et al., 2011).
Svtr	Gray-white very fine sandstone	Ripple cross bedding,	Unidirectional ripple migration under low flow conditions (Allen, 1965).
Svtw	Gray-white very fine sandstone	Wavy bedding, Mudstone bands	Influenced by alternating hydrodynamic conditions (Deng et al., 2025).
Mfsb	Grayish-green silty mudstone, mudstone	Bioturbation	Traces of the modification of sediments caused by biological activities (Ponce et al., 2024).

structures in distributary channels, with thicker sand bodies and coarser grain sizes (Zaman et al., 2012; Ta et al., 2014). The greenish muddy clasts (Se) indicate that the sediments were deposited in a reducing environment, with the gray-green mudstones from adjacent areas being eroded by river action and deposited in the distributary channel (Zhang L. et al., 2018). The gypsum clumps within the sandstone (Se) are also the result of allochthonous transport by the river (Wang et al., 2023).

4.1.1.2 Distributary bay and salt flat (FA2)

4.1.1.2.1 Description FA2 is primarily composed of gray-green mudstone (Figure 4), commonly associated with gypsum. Gypsum predominantly occurs as irregularly shaped nodules (Figures 4B–D) within the mudstone and can also fill fractures, with a clear boundary between the gypsum and mudstone. FA2 also contains dolomitic mudstone, with occasional small mud clasts (Figure 4A). Lenticular bedding of silty mudstone can be observed within

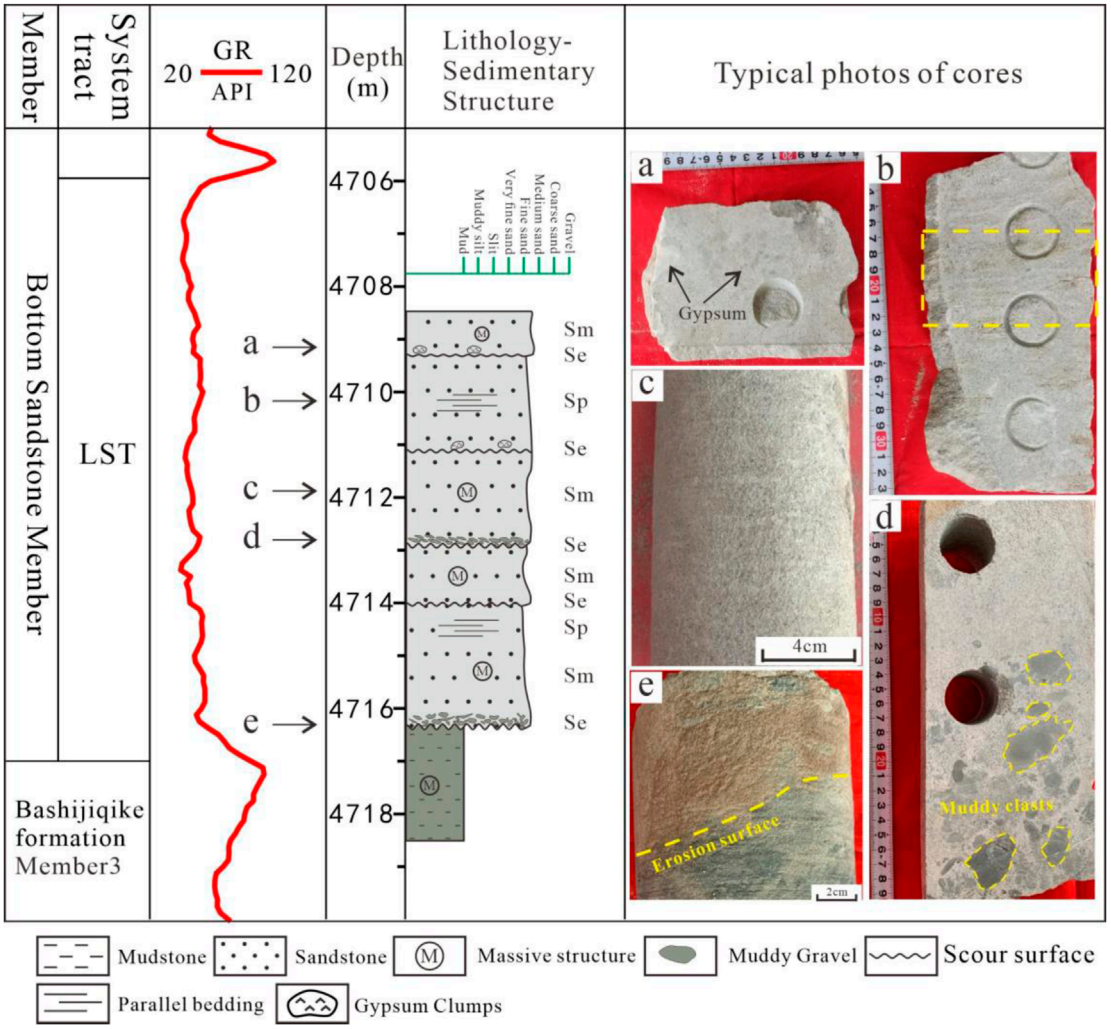

FIGURE 3
Lithological and sedimentary structural characteristics of the distributary channel in wellbore WM901. The drilling locations are shown in Figure 1C. **(A)** Grayish-white fine-grained sandstone, gypsum clumps on scour surfaces; **(B)** Grayish-white fine-grained sandstone, with crude parallel lamination; **(C)** Grayish-white fine-grained sandstone, massive structure with parallel lamination; **(D)** Grayish-white fine-grained sandstone, gray-green mudstone clasts scour surfaces; **(E)** Sharp, erosional surface between gray-green mudstone and grayish-white fine-grained sandstone.

the mudstone (Figure 4E). FA2 is primarily composed of the lithofacies Mm1, Mm2, DMm, and Ml.

4.1.1.2.2 Interpretation. FA2 is interpreted as distributary bay or salt flat deposits. The massive grayish-green mudstone (Mm2) represents a stable and low-energy reducing environment (Deng et al., 2025). The widespread occurrence of dolomitic mudstone and gypsum suggests that the deposition of the Bottom Sandstone Member occurred under relatively arid climatic conditions, formed through the continuous evaporation and concentration of brine (Li et al., 2017). The gypsum clumps (Mm1) in the grayish-green mudstone primarily formed during the early diagenetic stage (Luo et al., 2019; Wei et al., 2022). During the sedimentation process, when muddy detritus was rapidly deposited and buried, intense evaporation of surrounding water bodies caused the salinity of pore water to increase continuously, leading to the precipitation of calcium sulfate and other gypsum components from the solution. Gypsum gradually crystallized within the pores and microfractures of the mudstone. These pores and microfractures provided space for gypsum crystallization, and as the crystallization process continued, the gypsum crystals grew and aggregated, eventually forming gypsum clumps. The muddy clasts (DMm) in the dolomitic mudstone also represent corresponding flood events, transporting grayish-green muddy clasts and fine-grained terrestrial material to the dolostone sedimentary area (Du et al., 2020). Lenticular bedding (Ml) was formed by wave action transporting sandy sediments into FA2. These structures are common in subaqueous distributary bay mud deposits (Cai et al., 2022).

4.1.1.3 Delta front mouth bar (FA3)

4.1.1.3.1 Description FA3 is primarily composed of very fine-grained sandstone and fine-grained sandstone (Figures 5A–G). The lower portion of the sand bodies typically exhibits transitional bedding features, including muddy bands (Figures 5B, F)

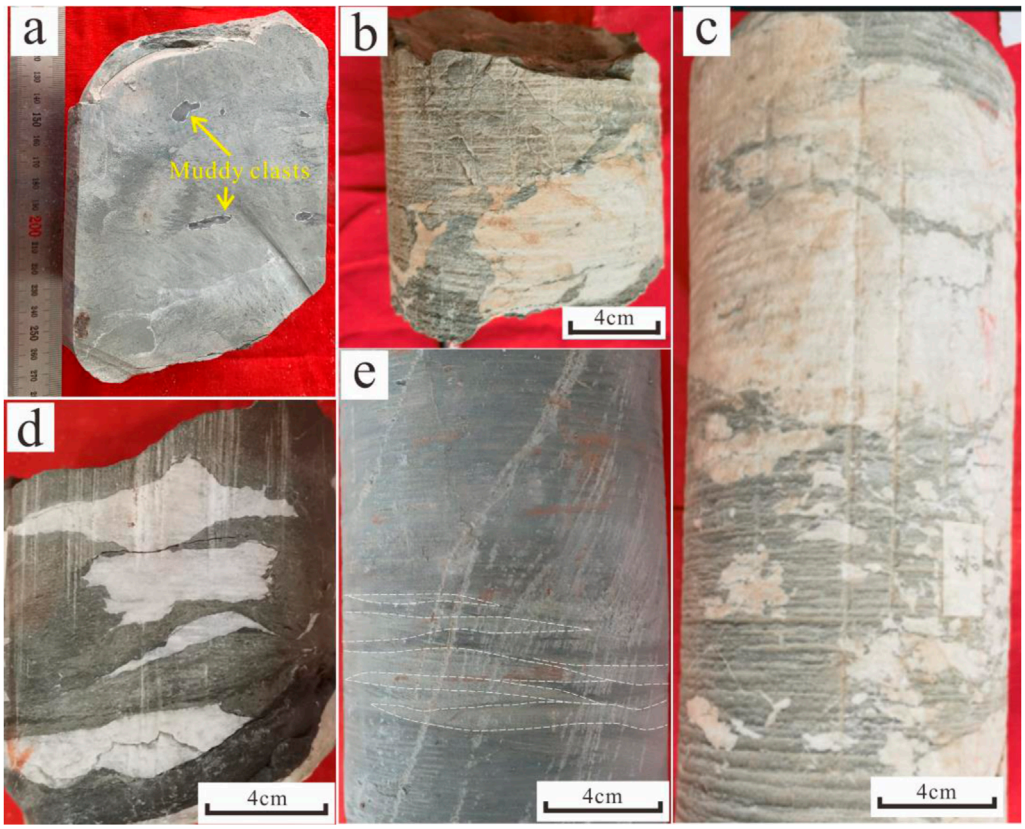

FIGURE 4
Core characteristics of the salt flat and distributary bay facies. **(A)** Wellbore WM9-1, 4704m, gray-green dolomitic mudstone, muddy clasts; **(B)** Wellbore WM11, 4,788.1m, gray-green mudstone, gypsum clumps, irregular gypsum; **(C)** Wellbore WM11, 4,788.5m, gray-green mudstone, gypsum clumps, irregular gypsum; **(D)** Wellbore WM23, 4,618.3m, gray-green mudstone, gypsum clumps, flat gypsum; **(E)** Wellbore WM231, 4,613.1m, gray-green mudstone, lenticular bedding of silty mudstone. The coring well locations are shown in Figure 1C.

and wavy bedding (Figure 5C), along with occasional flame structures (Figure 5G) and ripple lamination (Figure 5D). Moving upward, the sequence transitions into massive structures (Figure 5A). The bottom is characterized by bioturbated mudstone siltstone (Figure 5E). Overall, the sequence shows a coarsening-upward trend, and it commonly develops in association with FA1. The GR curve also displays a funnel-shaped pattern. The overall characteristics show a coarsening upward pattern, often interbedded with FA1. FA3 is primarily composed of the lithofacies Sm, Svtw, Svtr, and Mfsb. The GR curve also exhibits a funnel-shaped pattern.

4.1.1.3.2 Interpretation FA3 has relatively fine grain size, lacks scour structures, and exhibits an upward coarsening grain size trend, which can be interpreted as a mouth bar deposit (Cappelle et al., 2017). As river-borne sediments are deposited near the mouth, they form mouth bars. When the flow velocity decreases, fine-grained sediments are easily deposited on the flanks or behind the mouth bar, forming muddy bands and wavy bedding (Svtw) under the influence of waves and tidal action (Ponce et al., 2024). Flame structures (Svtf) are primarily associated with differential compaction of sediments. The delta front typically experiences higher energy and faster sedimentation rates. During rapid deposition, sediments may not have fully consolidated before being subjected to compaction by overlying sediments, leading to the Formation of flame structures (Taşgın et al., 2011). The development of massive structures (Sm) in the upper part of FA3 represents the rapid accumulation of later sediments (Arregui and Rodríguez, 2022). Bioturbation (Mfsb) refers to the disturbance of primary sedimentary structures by organisms living within the sediments. Controlled by hydrodynamics and organic matter content, this feature is commonly observed in mouth bar deposits (Ponce et al., 2024).

4.1.1.4 Delta front sheet sands (FA4)

4.1.1.4.1 Description FA4 is primarily composed of very fine sandstone, siltstone, muddy siltstone (Figures 6A–C). Muddy bands and wavy bedding (Svtw) are commonly observed (Figures 6B, C), along with bioturbation structures (Mfsb) (Figure 6A). The grain size shows an overall fine-coarse-fine grain size trend from bottom to top, with sediment thickness typically around 1–2 m. The GR curve exhibits a finger-shaped pattern.

4.1.1.4.2 Interpretation. FA4 is interpreted as sheet sand deposition (Deng et al., 2025). The grain size, bedding, and thickness of sheet sands are influenced by both wave and distributary channels. The sand bodies in distributary channels are affected by waves, causing lateral migration and forming sheet sand deposits

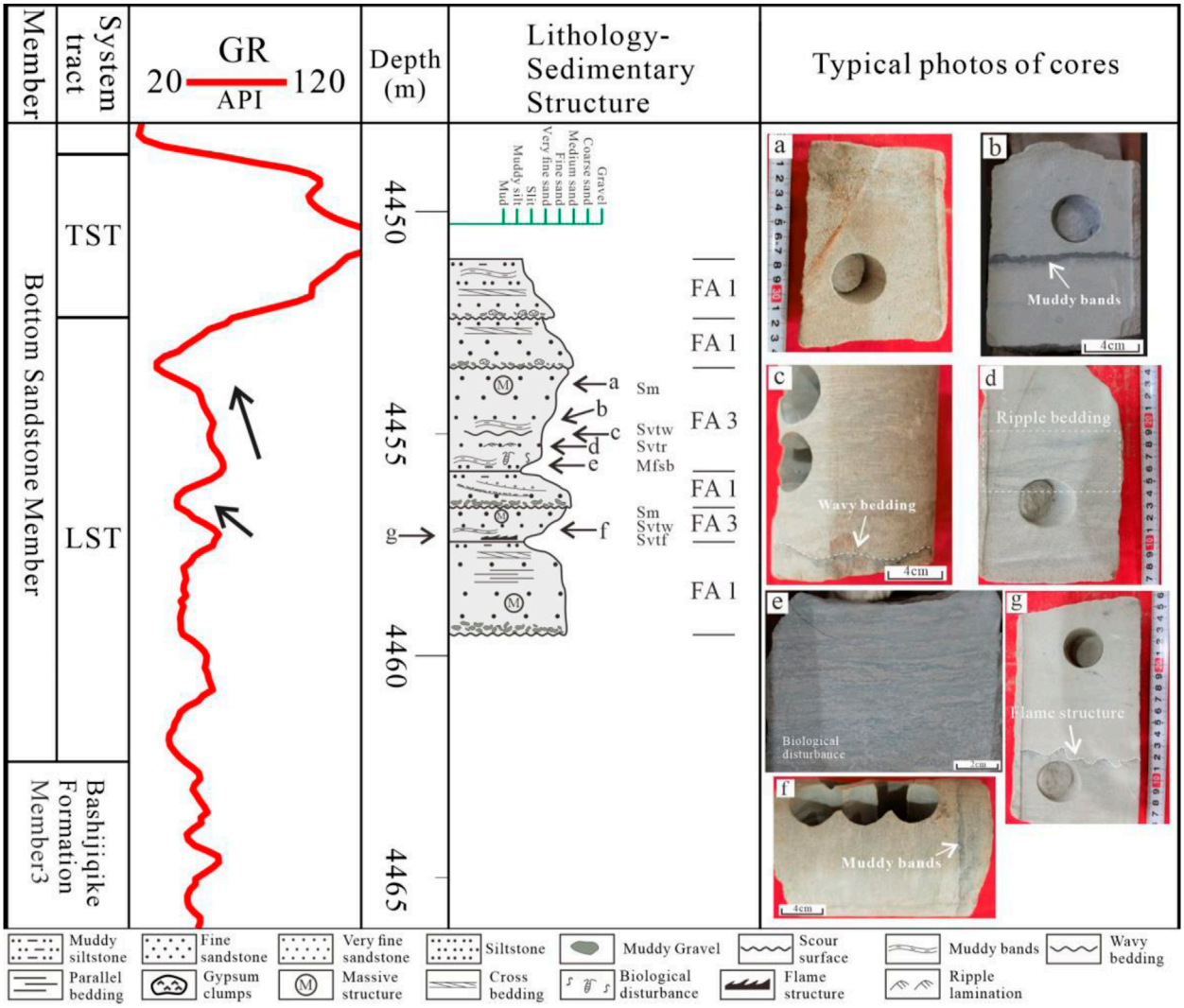

FIGURE 5
Lithology and sedimentary structure characteristics of the mouth bar FA3 in wellbore WM21. The mouth bar exhibits a coarsening-upward sedimentary sequence, with the GR value gradually decreasing upwards. The coring well locations are shown in Figure 1C. **(A)** Gray-white fine-grained, massive sandstone; **(B)** Gray-white very fine sandstone, mudstone bands; **(C)** Gray-white very fine sandstone, wavy bedding; **(D)** Gray-white very fine sandstone, small-scale ripple lamination; **(E)** Gray-green muddy siltstone, muddy bands, bioturbation; **(F)** Gray-white very fine sandstone, mudstone bands; **(G)** Gray-white very fine sandstone, flame structures.

commonly found in delta front environments (Qin et al., 2020). Intense wave action leads to the mixing of mud-rich sediments with sand bodies, resulting in the Formation of wavy bedding and muddy bands (Svtw) (Deng et al., 2025). Due to the finer grain size of the sheet sands, the hydrodynamics during deposition were relatively weak, allowing for the development of biological activity (Mfsb) (Arregui and Rodríguez, 2022).

4.1.2 Saline lake (FA5)

4.1.2.1 Description

FA5 is primarily composed of grayish-green gypsum-rich mudstone (MG), mudstone (Mm2), and white gypsum (Gm). Among them, the gypsum-rich mudstone has a relatively high gypsum content, with unclear boundaries between gypsum and mudstone. The gypsum and mud deposits are mixed, resulting in a high degree of heterogeneity in the rock (Figures 7A, B). Layered gypsum and mudstone (Figures 7C, D) are also present, exhibiting a massive structure, with both types interbedded and showing sharp contacts. The gypsum-rich mudstone and gypsum show characteristics of low GR and high resistivity on the well log(Figure 7E), while the mudstone exhibits high GR and low resistivity (Figure 7F).

4.1.2.2 Interpretation

FA5 is interpreted as a saline lake deposit. The gypsum-rich mudstone (MG), where gypsum and mudstone are mixed, indicates that the mud deposits were co-deposited with gypsum. This lithofacies mainly formed in a shallow saline lake environment, where, as the saline lake evaporated, the water salinity continuously increased, leading to the gradual

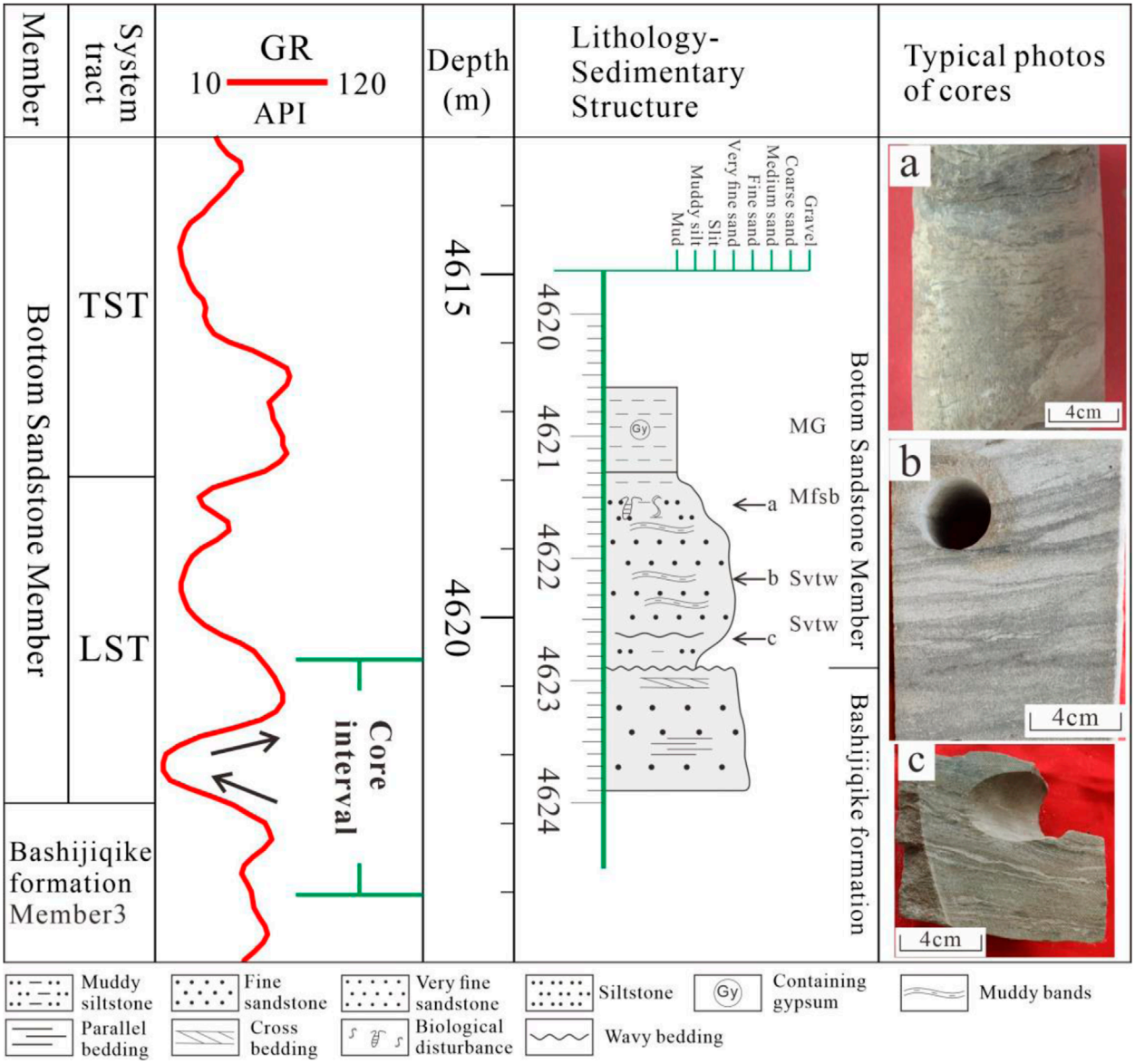

FIGURE 6
Lithology and sedimentary structures of sheet sands in wellbore WM23. The coring well locations are shown in Figure 1C. **(A)** Gray-green silty mudstone, bioturbation structures; **(B)** Gray-green very fine sandstone, mudstone bands; **(C)** Gray-green very fine sandstone, wavy bedding.

crystallization and precipitation of gypsum. During this process, wave and tidal actions brought in fine-grained material, which was deposited alongside the gypsum, forming gypsum-rich mudstone (Zhuo et al., 2018; Wang et al., 2020).

The massive gypsum (Gm) and mudstone (Mm2) suggest that the water was relatively calm during deposition. The interbedded gypsum and mudstone primarily reflect the influence of paleoclimate and lake level changes (Wu et al., 2024). Due to the extreme aridity in the study area, terrestrial input was relatively weak during the dry season, while the basin continued to evaporate and concentrate, causing the saline lake salinity to rise. In the shallow lake area, layered gypsum could form. When the rainy season arrived, terrestrial input increased, lake levels rose, and water salinity decreased, with mud deposits dominating in the shallow lake area.

4.2 Characteristics of faults

4.2.1 Seismic expression of faulting

Based on the interpretation of the Paleogene basal boundary (E_b) and the top boundary of the Bottom Sandstone Member in the seismic profile perpendicular to the WM7 fault zone, it is found that the WM7 fault zone primarily develops normal faults. There is a certain thickness variation in the strata on both sides of the fault (Figure 8A). The strata on the downthrown block are thicker than those on the upthrown block, with multiple graben and half-graben combinations developed (Figure 8A). However, the thickness difference of the strata is relatively small, and the overall structure consists mainly of small-scale syndepositional faults (Dou et al., 2020a; 2020b).

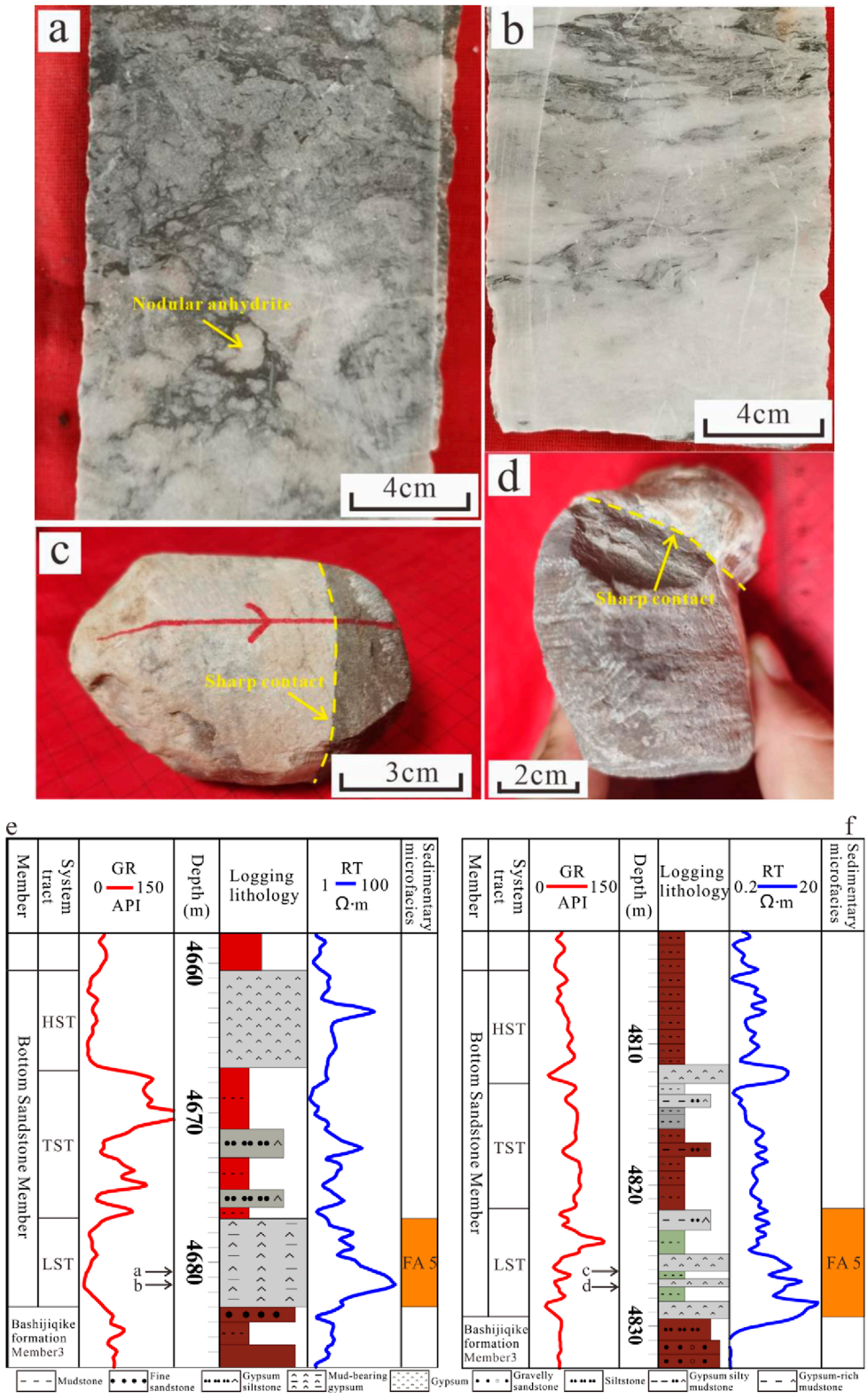

FIGURE 7
Core and logging curve characteristics of the saline lake. Core locations are shown in Figures 7E,F, The drilling locations are shown in Figure 1C. **(A)** Wellbore WM16, 4,680.6 m, gypsum-rich mudstone, with nodular anhydrite present, indistinct boundary between gypsum and mudstone; **(B)** Wellbore WM16, 4,681.5 m, gypsum-rich mudstone, indistinct boundary between gypsum and mudstone; **(C)** Wellbore WM61, 4,826 m, laminated gypsum, underlain by gray-green mudstone, sharp contact; **(D)** Wellbore WM61, 4,827.2 m, gray-green mudstone, overlain by gypsum, sharp contact. **(E)** Wellbore WM16, the lowstand systems tract consists of saline lake deposits, characterized by gypsum-rich mudstone; **(F)** Wellbore WM61, the lowstand systems tract consists of saline lake deposits, characterized by laminated gypsum and gray-green mudstone.

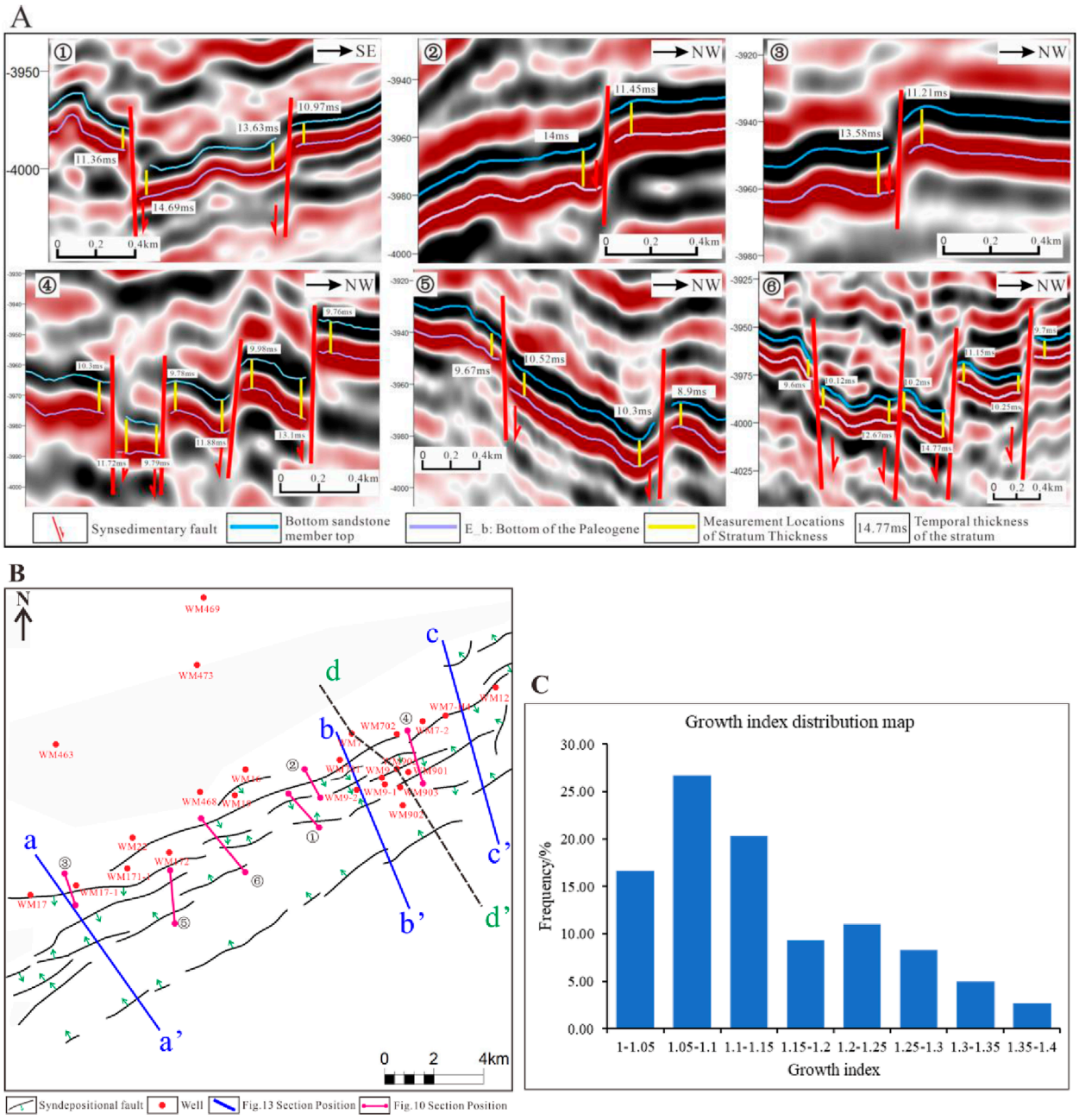

FIGURE 8
Fault characteristics of the WM7 fault zone **(A)** Seismic profile perpendicular to the WM7 fault zone, with the profile location shown in **(B)** ①~⑥. By measuring the seismic temporal thickness on both sides of the faults, it is found that the normal faults in the study area are mainly small-scale syndepositional normal faults. The thickness of the strata in the downthrown block is greater than that in the upthrown block, and they mostly occur in the form of graben or half-graben combinations **(B)** Distribution characteristics of syndepositional faults, exhibiting an echelon-like pattern **(C)** The distribution characteristics of the growth index of syndepositional faults. Growth index = h_d/h_u, h_d: Downthrown block stratigraphic thickness; h_u: Upthrown block stratigraphic thickness.

These syndepositional faults will be the main focus of this study.

Through fault interpretation, it was found that the overall strike of the syn-sedimentary faults is southwest-northeast, and they exhibit an echelon-like planar arrangement (Figure 8B). The individual fault lengths range from 0.5 km to 12 km, with an average of 3,418.6 m length. By measuring the stratigraphic thickness on both sides of the syndepositional faults in multiple seismic profiles and calculating the growth index of the syndepositional normal faults, it was found that the growth index is primarily distributed between 1–1.4, with an average of 1.14 (Figure 8C). This indicates that the activity of the syndepositional faults is relatively weak, and they are small-scale syndepositional normal faults. The faults on both sides of the fault zone dip toward the center, resulting

in the Formation of a large graben along the WM7 fault zone, within which a complex syndepositional fault combination style develops (Figure 8B). The syndepositional fault combinations within the graben can be classified into three types: wall-corner style, domino-style, and graben-horst (Figure 9). The wall-corner style fault combination is characterized by relatively higher terrain near the fault, with the stratigraphic dip on one side opposite to the fault dip, while the stratigraphic dip on the other side is in the same direction as the fault dip. The overall dip of the strata on both sides forms an obtuse angle (Figure 9A). The domino-style fault combination consists of multiple half-graben structures with the same dip direction. The syndepositional faults have consistent dip directions, while the strata dip in the opposite direction to the faults (Figure 9B). The graben-horst combination is relatively less developed in the study area, typically consisting of a graben and a horst. This combination is commonly found on the left side of the WM7 fault zone in the study area (Figure 9C).

4.2.2 Structural and stratigraphic characteristics of WM7 fault zone

Seismic interpretation of the top boundary of the Bottom Sandstone Member, the Paleogene base, the bottom boundary of the Gypsum Mudstone Member, and the bottom boundary of the White Sandstone Member was conducted based on well-seismic calibration. The Paleogene base can be traced throughout the entire area, representing a regional unconformity (Zhang et al., 2021). In contrast, the Cretaceous strata exhibit relatively weak seismic amplitude and poor continuity of seismic reflectors, which starkly contrasts with the seismic reflections of the Paleogene base (Figure 10A). The Bottom Sandstone Member gradually onlap and thins from the northwest to the southeast, with its distribution covering the WM7 fault zone. The White Sandstone Member gradually thins and pinches out near the WM7 fault zone, from southeast to northwest (Figure 10A). The well correlation profiles also show this characteristic (Figure 10B).

Comparison of well-seismic profiles reveals that the WM7 fault zone exhibits an overall topographic pattern of southeast high and northwest low. The Bottom Sandstone Member is developed only within the WM7 fault zone and its western part, while the eastern White Sandstone Member was exposed at the surface and eroded during the deposition of the Bottom Sandstone Member. Influenced by syndepositional fault activity, the WM7 fault zone developed a large graben, with a relative thinning of seismic axis thickness in the western block near the fault zone, forming a syndepositional uplift (Figure 10A), which collectively controls the distribution of the topographic features.

This study constructs a residual thickness map based on seismic stratigraphic interpretation to characterize the geomorphic development features of the WM7 fault zone. Due to the gradual pinching out of the Bottom Sandstone Member to the east, it is difficult to represent the geomorphic features of the entire study area during sedimentation. However, the seismic axis of the bottom boundary of the Gypsum Mudstone Member covers the entire study area (Figure 10A) and is approximately parallel to the Bottom Sandstone Member. A residual thickness map was constructed using the bottom boundaries of the Gypsum Mudstone Member and the Bottom Sandstone Member of the Paleogene. Based on this map, the geomorphic features of the Bottom Sandstone Member during sedimentation can be inferred (Figure 11A). Seismic stratigraphic interpretation reveals the development of numerous incised valleys near the base of the Paleogene in the eastern part of the WM7 fault zone (Figure 11B) (Wang, 2015; Xia et al., 2022). These incised valleys are approximately perpendicular to the WM7 fault zone, suggesting that during deposition of the Bottom Sandstone Member, rivers transported clastic materials from the eastern White Sandstone Member to the WM7 fault zone for deposition. The scale of a single river channel in the study area was measured, with its width ranging from 250 m to 1,000 m, with an average of 610 m. The channel thickness ranges from 15 m to 40 m, with an average of 28 m.

As shown in the residual thickness map (Figure 11A), the WM7 fault zone is a large graben developed at the location of the slope-break zone. The graben contains numerous small-scale syn-sedimentary normal faults (Figure 8B), with the slope gradually flattening from east to west. A large number of incised valleys have developed in the southeastern uplift of the WM7 fault zone. These incised valleys converge near the southeastern boundary of the WM7 fault zone (the white dotted line in the southeastern part of Figure 11A) and extend into the fault zone, indicating that the fault has a certain controlling effect on the incised valleys.

4.3 Sedimentary facies distribution

Based on sedimentary facies identification, the distribution characteristics of sedimentary facies were analyzed using 3D seismic data and seismic sedimentology techniques (Zhu et al., 2020). Seismic sedimentology, as an interdisciplinary field integrating seismology and sedimentology, serves as a high-resolution complement to traditional low-resolution seismic stratigraphy. Its core lies in utilizing seismic data to thoroughly analyze sedimentary characteristics and evolutionary patterns (Zeng et al., 2012; Zeng, 2018). Among its key techniques, stratal slicing plays a crucial role. This method, based on chronostratigraphic surfaces, enables an accurate depiction of the planar distribution of sedimentary bodies within the same depositional period (Zeng et al., 2012; Zeng, 2011).

Based on the detailed interpretation of the top and bottom boundaries of the Bottom Sandstone Member, the maximum amplitude attribute is extracted and analyzed in conjunction with geomorphological features to investigate the distribution patterns of sedimentary facies. Given the thickness variations of strata on both sides of synsedimentary faults, proportionally scaled stratal slicing is applied under the constraint of top and bottom surfaces to prevent slicing across layers and ensure the isochronous nature of the slices. The relationship between maximum amplitude attributes and sand body thickness (Figure 11C) indicates a connection between amplitude and sand body characteristics. The facies distribution exhibits significant facies variability, as evidenced by the distribution of fan bodies (Figure 11D). The analysis suggests that sand bodies are relatively well-developed in the eastern part of the fault zone, gradually thinning westward until they pinch

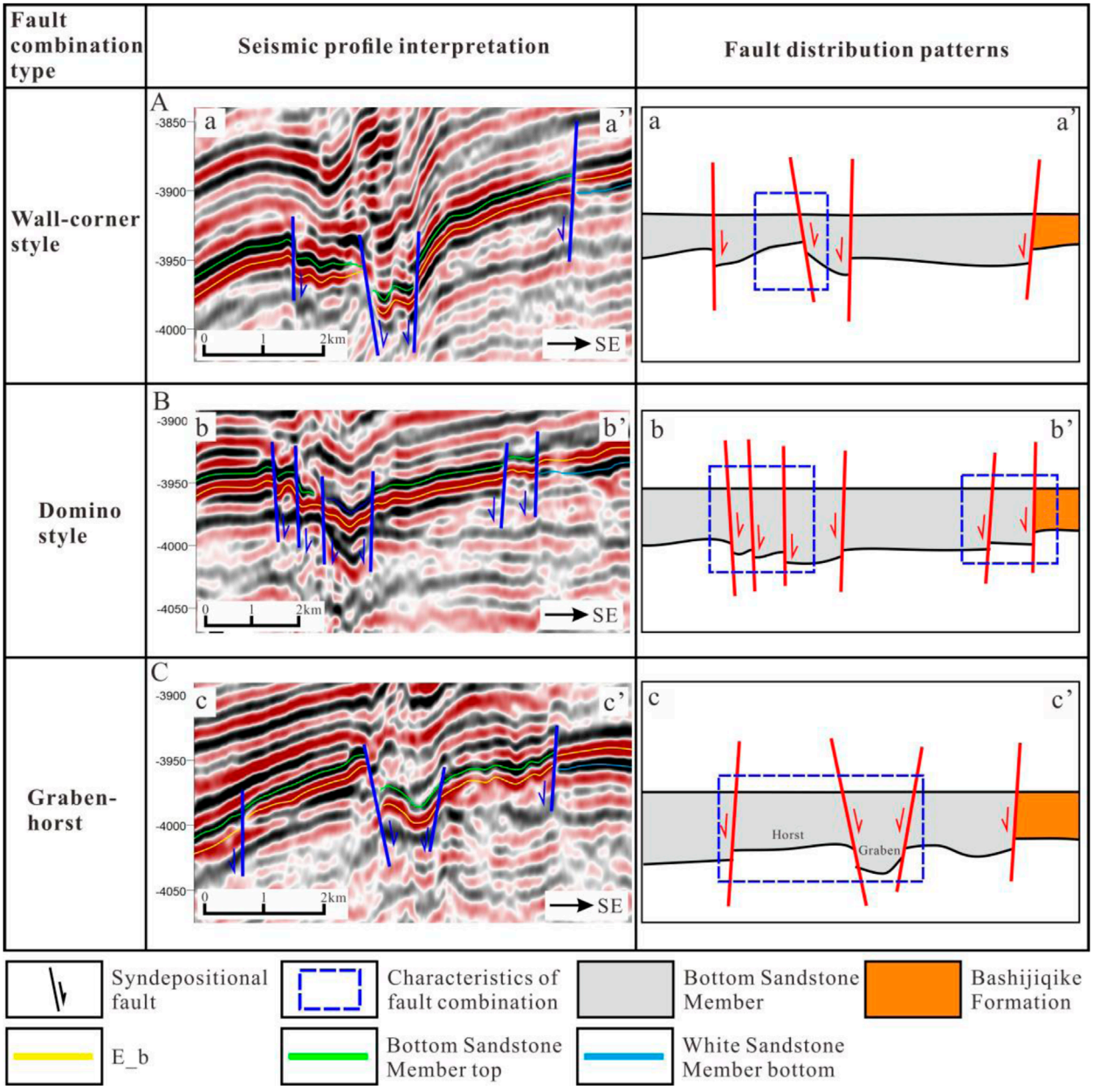

FIGURE 9
Distribution characteristics of syndepositional faults in the WM7 fault zone (location of seismic profile shown in Fig. 8B). **(A)** Seismic profile of wall-corner style syndepositional faults; **(B)** Seismic profile of domino style syndepositional faults; **(C)** Seismic profile of Graben-horst syndepositional faults. The sketch on the right illustrates the relative stratigraphic thickness after the top boundary of the Bottom Sandstone Member has been flattened.

out. In some areas, sand bodies can breach the fault zone and extend relatively far, as observed near wellbores WM7 and WM17 (Figure 11D). The distributary channels within the fault zone exhibit significant deflections near the fault. Additionally, based on lithology from drilling data, it was observed that the development of gypsum rocks increases gradually from east to west within the fault zone, while the gypsum content decreases progressively closer to the center of the lacustrine basin (Figure 11D). The distribution characteristics of this sedimentary facies can be used to interpret the sedimentary infill patterns within the complex fault blocks.

5 Discussion

5.1 Genetic analysis of the graben zone at the slope-break zone

Tectonic activity plays a crucial role in the Formation and evolution of paleogeography (Li et al., 2019; Jiang et al., 2022). Since the Late Cretaceous, influenced by the remote effects of the India-Eurasia plate collision, the South Tianshan Orogenic Belt was reactivated and began to gradually uplift. During this period, the northern Tarim Basin experienced basin flexure and subsidence

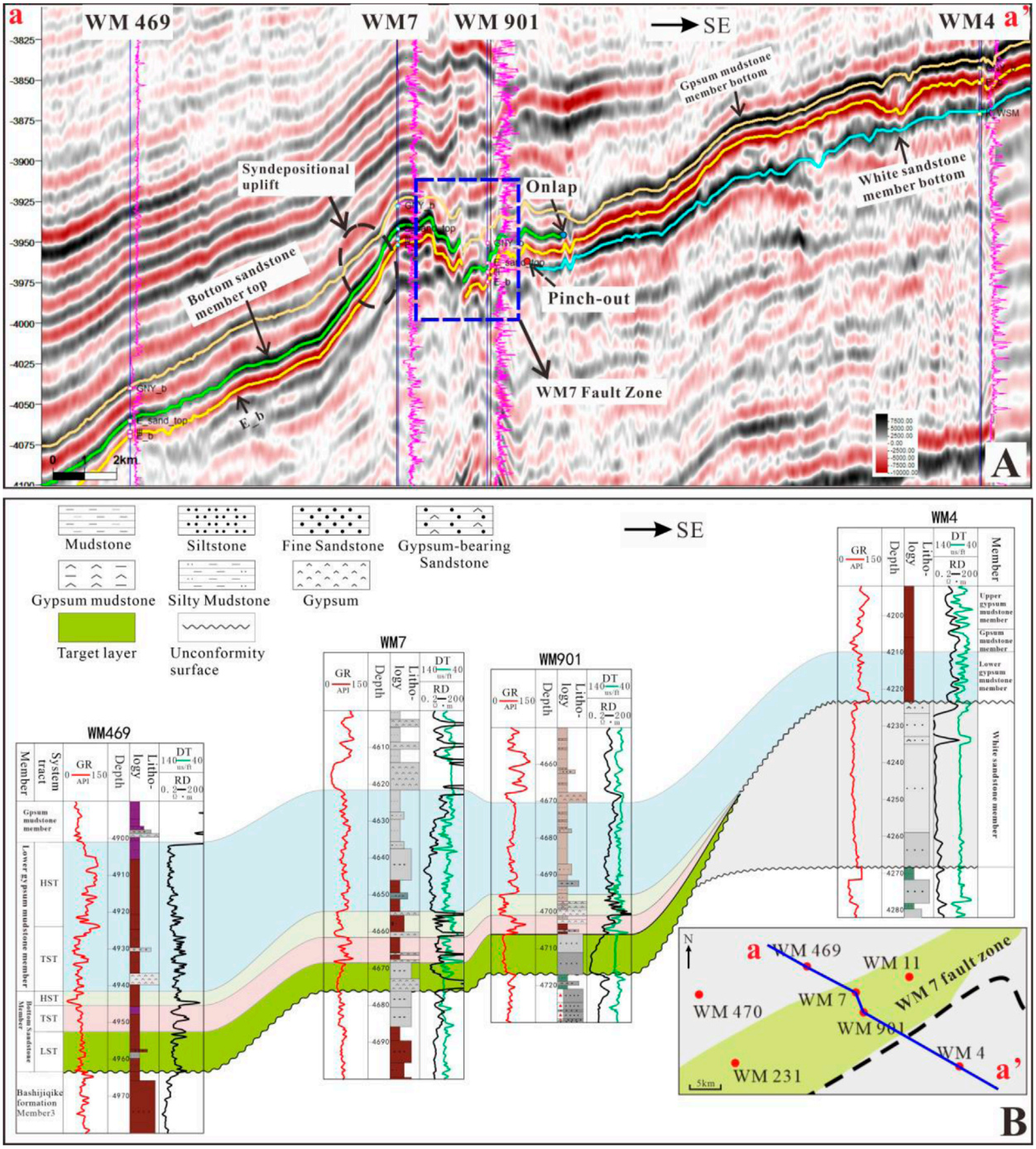

FIGURE 10
Well-to-seismic profile of wellbores WM469- WM4 **(A)** Seismic section across the WM7 fault zone, where the seismic axis of the Bottom Sandstone Member gradually onlap and thins from northwest to southeast, while the seismic axis of the White Sandstone Member gradually thins and pinches out from southeast to northwest. The lower Gypsum Mudstone Member blankets the entire area **(B)** Corresponding inter-well cross-section for Figure 10A, where the Bottom Sandstone Member progressively thins from northwest to southeast.

(Kuqa Depression-Tabei Uplift) due to the thrusting and imbrication of the South Tianshan Orogenic Belt (Jin et al., 2005; Zhang et al., 2014; Chen et al., 2024). In contrast, the southern Kunlun Orogenic Belt, affected by plate collision and accretion, was compressed northward, leading to the gradual uplift of the southeastern Tarim Basin during the Late Cretaceous-Paleogene, with no sedimentation occurring in this area (Ding et al., 1996; Yang et al., 2007; Wu G. et al., 2020). Under the influence of flexural subsidence in the northern Tarim Basin and the relative uplift of the strata in the southeastern region, the Tabei Uplift manifests as a northward-dipping slope. The subsidence center of the Tabei Uplift has gradually migrated northward (Ding et al., 1996; An et al., 2009; Zhang et al., 2022),

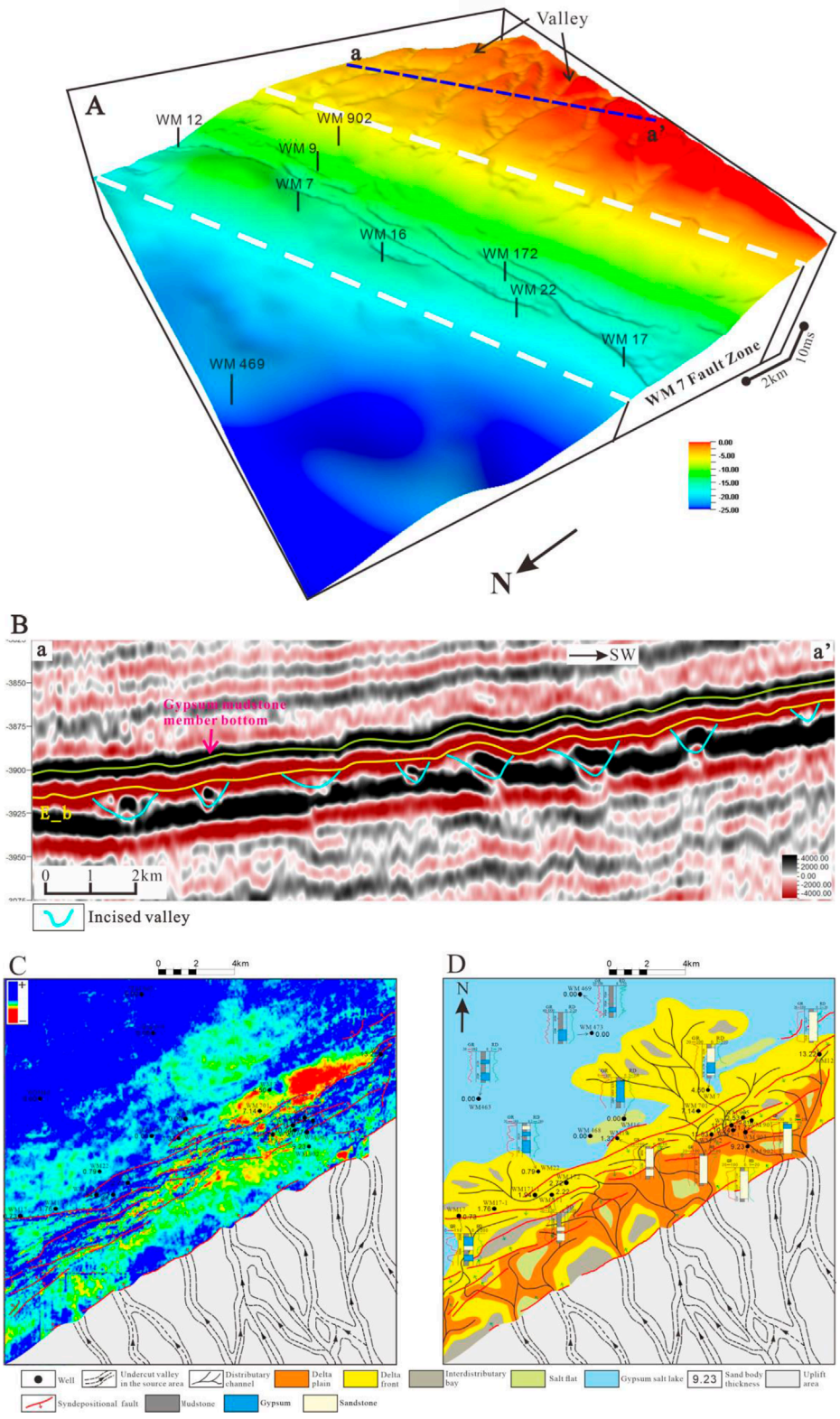

FIGURE 11
(A) A residual thickness map is created from the bottom boundaries of the Gypsum Mudstone Member and the Paleogene. The area between the white dashed lines represents the WM7 fault zone. The eastern part of the fault zone is exposed at the surface as White Sandstone Member **(B)** Seismic profile parallel to the fault zone. Numerous seismic reflections of river-incised valleys are developed near the Paleogene boundary. The location of the profile is shown in **[(A) a-a']** **(C)** Maximum amplitude attribute. By comparing the thickness of sand bodies, it is found that sand bodies in warm-colored regions are thicker, while those in cool-colored regions are thinner **(D)** sedimentary facies distribution map of the study area. The seismic data used are high-quality 3D seismic data from a small area. The extent of the map corresponds to the range of the seismic data (Figure 1C, blue dashed box).

resulting in a geomorphological pattern characterized by higher elevations in the southeast and lower elevations in the northwest in the study area. Additionally, differential subsidence occurred due to the influence of basement uplift, leading to the Formation of a slope-break zone along the WM7 fault zone (Figure 11A).

Through the analysis of seismic profiles perpendicular to the WM7 fault zone, it was found that the WM7 fault zone was influenced by basement activity and magma intrusion prior to the Cretaceous deposition (Chen et al., 1998; Yang et al., 2005), resulting in the Formation of two magmatic ancient uplifts (Figure 12B, black box, the chaotic reflections beneath the Cretaceous are magmatic rocks). Additionally, numerous reverse faults developed (Figure 12B, red faults). The reverse fault was primarily formed by oblique collision and oblique-slip during the South Tianshan Orogeny at the northern margin of the Tarim Plate in the late Hercynian, resulting in a NE-trending en echelon distribution of the faults (Wei et al., 1995; Wei et al., 2001; Chen et al., 2009). The intrusion of magmatic rocks primarily occurred during the late Hercynian, and the Formation of numerous reverse faults led to the development of a "basement structural weakness zone" in the study area, which controls the development of overlying normal faults (Tang et al., 1999; Wei et al., 2001; An et al., 2009).

During the Mesozoic-Cenozoic, influenced by the South Tianshan collision orogeny and the Himalayan collision orogeny, the Tabei Uplift entered a stress relaxation stage, leading to subsidence of the strata. A series of extensional structures composed of normal faults were formed during this period, exhibiting an en echelon arrangement and a graben-horst structure or stair-step normal fault combination in the profile (Yang et al., 2000; Zhao et al., 2012; Li et al., 2013; Du et al., 2024). Previous studies have divided the Formation of extensional structures into two phases based on their timing. The first phase is the extensional structures developed during the Jurassic to Early Cretaceous, primarily in the southeastern part of the Tabei Uplift and the eastern part of the Lunnan Low Uplift (Zhao et al., 2012). No significant changes in strata thickness were observed near the faults in the WM7 fault zone (Figure 12A, blue box), indicating that the normal faults in the Early Cretaceous strata of the WM7 fault zone formed after deposition. The second phase occurred during the Late Cretaceous to Neogene, when the collision between the Indian Plate and the Eurasian Plate caused north-south-directed compressional forces on the Tarim Basin. This resulted in a transtensional stress field affecting the Tabei Uplift, where a transtensional fault system developed in the western part of the Tabei Uplift (Zhao et al., 2012; Li et al., 2013). The extensional component is related to the tectonic and sedimentary loading experienced during the migration of the subsidence center to the north (Yang et al., 2000; Zhang et al., 2017). During the Late Cretaceous subsidence, the WM7 fault zone, influenced by the previously existing "basement structural weakness zone," generated local extensional stress. According to Anderson's normal faulting model (Yu and Lu, 1986), the Cretaceous strata of the WM7 fault zone slipped downward, forming a series of normal faults and graben structures (Figure 12B, blue faults). The development of normal faults in the Cretaceous strata within the WM7 fault zone is relatively more pronounced, with a higher degree of stratigraphic fragmentation. In contrast, the fault development is relatively less pronounced in the coeval sedimentary uplift areas (Figure 12B, blue faults). This is likely due to the fact that the magmatic uplift in the syndepositional uplift areas is closer to the central part of the entire magmatic diapir (Cheng et al., 2010), where the basement rocks possess higher mechanical strength, making them less prone to fracturing and deformation, and thus experiencing lower subsidence. On the other hand, the WM7 fault zone is closer to the periphery of the magmatic diapir (Cheng et al., 2010), where the surrounding lithology consists mainly of early clastic rocks with relatively lower mechanical strength. During the subsidence process, the reverse faults in the basement are more prone to slipping.

During the deposition of the Bottom Sandstone Member, the normal faults within the Cretaceous strata of the WM7 fault zone (Figure 12B, blue faults) developed to a greater extent, leading to a higher degree of stratigraphic fragmentation and lower rock mechanical strength. Under the combined control of the "basement structural weakness zone," local extensional stresses persisted during the subsidence process. Compared to the surrounding strata, the subsidence was greater, forming a large graben with multiple small-scale syndepositional faults within it (Figure 12B, black faults). In contrast, in the western part of the wellbore WM7, due to the influence of the basement uplift, the subsidence was relatively small, resulting in the Formation of a syndepositional uplift during the differential subsidence process (Figure 12B, red box).

The torsional component occurs under the near north-south compressive stress in the basin, along the northwest boundary of the rhombic-shaped Tarim Basin, producing a near NEE-directed left-lateral shear force. This reactivates the near NEE-oriented faults, formed during the pre-Mesozoic in the northern Tarim Uplift, leading to left-lateral twisting (Yang et al., 2000). Influenced by the en echelon fault assemblage formed in the Pre-Mesozoic, the normal faults in the Mesozoic-Cenozoic strata exhibit some inheritance, are arranged in an en echelon pattern, and also exhibit strike-slip characteristics (Figure 8B).

In summary, during the Late Cretaceous to Paleogene, under the remote effect of the India-Eurasia plate collision, the northern Tarim Uplift developed a geomorphological pattern with higher elevations in the southeast and lower elevations in the northwest during the deposition of the Bottom Sandstone Member. During the differential subsidence process, the study area developed geomorphological features of "syndepositional normal faults-graben-slope."

5.2 Effect of syndepositional faults on sand bodies

5.2.1 The distribution and control mechanisms of incised valleys

During the deposition period of the Bottom Sandstone Member, the White Sandstone Member in the eastern part of the WM7 fault zone was in an erosion zone, forming an unconformity. Numerous incised valley deposits developed near this sequence boundary. The formation of incised valleys resulted from the river's sediment transport capacity exceeding sediment supply, and the associated incised valley deposits are typically closely related to relative sea-level or lake-level fall (Boyd et al., 1994). Due to the significant reduction in accommodation space, these sedimentary records serve as key indicators for identifying sequence boundaries (Boyd et al., 2006). Tectonic activity and climate change are major controlling factors in the formation of incised

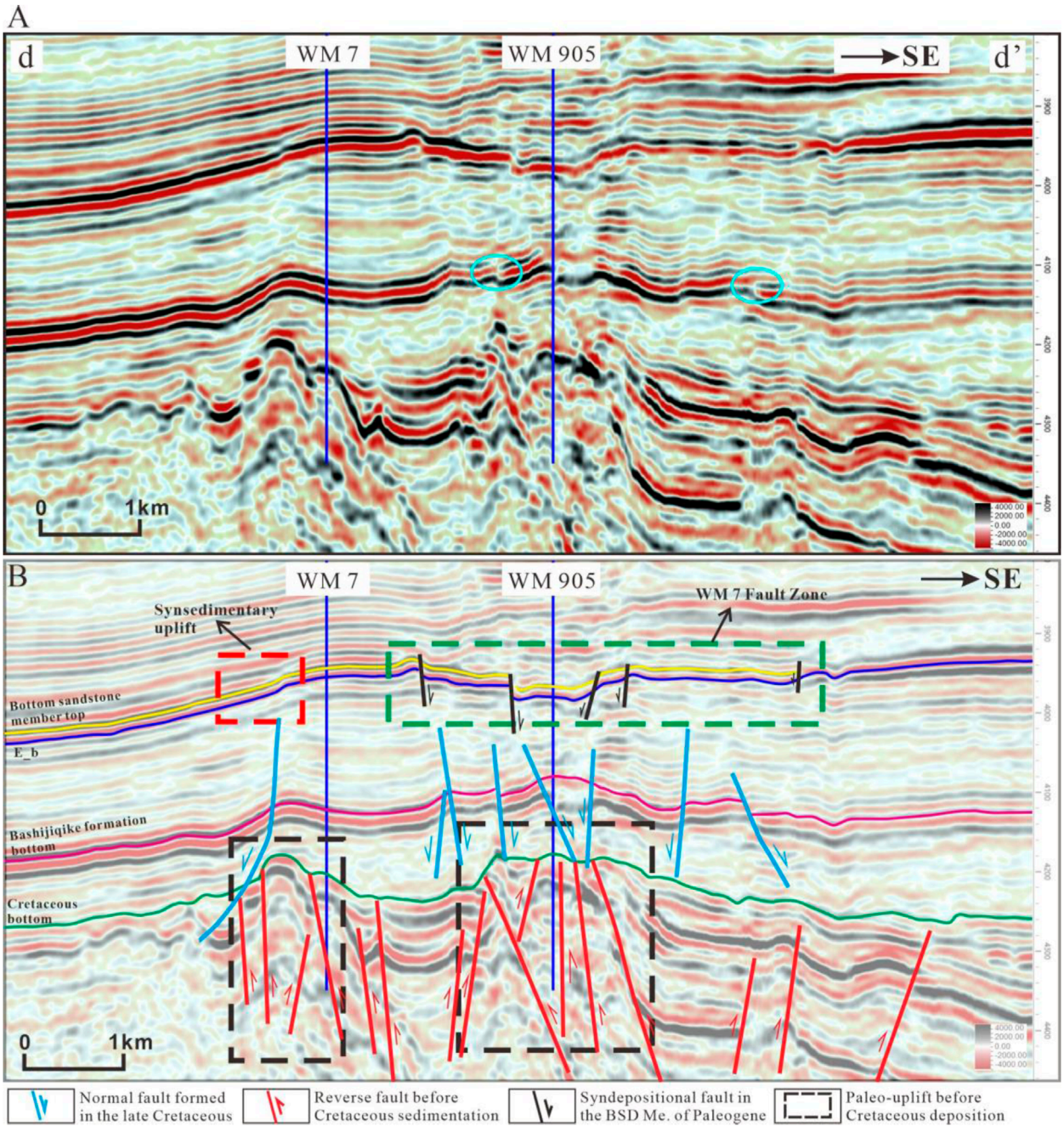

FIGURE 12
Fault development characteristics of the WM7 fault zone. **(A)** Seismic profile of wellbores WM7–WM901, with profile location shown in Fig. 8B (d–d'). **(B)** Interpretation of the seismic horizons and faults in Fig. 12A The black faults are syndepositional faults from the Paleogene; the blue faults are normal faults formed under the influence of stratigraphic subsidence during the Late Cretaceous; the red faults are reverse faults formed prior to Cretaceous deposition due to magmatic activity.

valleys. Tectonic movements alter regional topography and slope conditions, controlling where sediments transported through sediment pathways are unloaded and deposited in specific areas (Harishidayat et al., 2018; Kiswaka et al., 2024; Chavanidis et al., 2024). Meanwhile, climate influences variations in water discharge and sediment supply (Boyd et al., 2006; Dalrymple et al., 2006). Previous studies have extensively investigated incised valleys in marine basins, particularly in locations along continental slopes and shelf margins (Kiswaka et al., 2024; Harishidayat et al., 2024). The formation of shelf-margin incised valleys is primarily controlled by sea-level changes and fluvial erosion, closely associated with the lowstand systems tract in sequence stratigraphy (Dalrymple et al., 2006; Kiswaka et al., 2024). In contrast, incised valleys near continental slopes are mainly influenced by gravity flows and tectonic activities (such as faulting and landslides) (Fildani, 2017; Harishidayat and Raja, 2022). In continental lacustrine basins,

the formation of incised valleys is highly sensitive to climate changes, particularly under the arid to semi-arid conditions of the study area (Zhu, 2000; Qin et al., 2021). During the deposition of the lowstand systems tract in the Bottom Sandstone Member, large-scale deltaic deposits developed along the WM7 fault zone (Figure 11D), indicating high precipitation, strong terrigenous sediment supply, and lower aridity. This, in turn, facilitated the formation of numerous incised valleys in the source area. In contrast, during the transgressive to highstand systems tract, the study area was predominantly characterized by saline lake deposits. Compared to the lowstand systems tract, the lake basin expanded (Chen et al., 2017), with the primary deposits consisting of gypsum-rich mudstone and gypsum (Figure 10B), and no extensive deltaic deposits were observed. Consequently, during this period, the White Sandstone Member in the eastern WM7 fault zone remained exposed at the surface and was not subjected to significant fluvial erosion to transport clastic material into the study area. The expansion of the lake basin was primarily controlled by tectonic subsidence (An et al., 2009; Zhang et al., 2022). However, during this time, aridity gradually intensified, rivers were not well developed, and incised valleys were likely filled with eolian sand deposits (Ta et al., 2014).

Topographic features control the morphology and flow direction of incised valleys (Larsen et al., 2023), especially in areas with fault activity (Harishidayat et al., 2018). Under the activity of the syndepositional normal faults in the study area, a fault slope break zone was formed (Figure 14C). At the slope break, there are differences in water depth, and hydrodynamics which control the distribution of sand bodies through unloading processes (Feng, 2006). The easternmost part of the WM7 fault zone is composed of a series of syn-depositional faults with consistent dip and strike. The stratum of the Bottom Sandstone Member pinches out at this location, thus serving as an approximate boundary between the erosion zone and the deposition zone (Figure 13A). As shown in Figure 13, the location of valley development near the faults is correlated with the degree of fault development. For example, at Fault F1, the valley intersects with the location of Profile ②, where the displacement of the syndepositional fault at profiles ② is relatively lower compared to profiles ① and ③. Similarly, at Fault F2, it can be observed that the displacement of the syndepositional faults gradually decreases from the southwest-northeast direction (Figure 13B ④~⑥), with the river channel preferentially passing through the location of profiles ⑤~⑥.

A similar case can also be found in modern sedimentation. In the northern part of Zhangnaicuo lake, Nima County, Tibet, a series of syndepositional faults with consistent strike and dip are developed (Figure 13C). Through the analysis of valleys and faults, it was found that valleys intersect the faults at locations with relatively low fault displacement, where clastic rock deposits are formed on the downthrown side. Although valleys also develop at locations with larger fault displacements, the valleys are smaller in scale, with a shorter length, and no large-scale clastic rock deposits are formed (Figure 13C'). Due to the relatively dense valley development in this area, the clastic rock deposits are laterally interbedded and relatively continuous. A similar geological landscape has also been found in the southeastern part of Daihai, Inner Mongolia, China (Figure 13D). The valley similarly intersects the syndepositional fault at locations with relatively low displacement, where clastic rock deposits are formed on the downthrown side (Figure 13D'). Additionally, at the far left and far right of Figure 13D', the river channels converge and pass through the syndepositional fault at locations with smaller displacements.

By comparing the development characteristics of incised valleys and syndepositional faults, and integrating modern sedimentation observations, it is found that in the erosion zone, when the river flow direction aligns with the fault dip, valleys tend to converge and pass through the syndepositional fault at locations with relatively low fault displacement on the fault's upthrown side. Then, as the hydrodynamics decrease on the fault's downthrown side, sediment unloading occurs, forming clastic rock deposits, after which clastic material continues to accumulate forward under the influence of river dynamics.

5.2.2 Control of syndepositional fault-grabens-slope on sand bodies

The undulation of the terrain also controls the migration path and distribution pattern of sediments. When sediment flows encounter topographic obstacles such as highlands and fault scarps, their movement will be hindered, resulting in a rapid decrease in flow velocity and the accumulation of particles in front of the obstacles, forming specific sedimentary bodies. In addition, topographic obstacles can also change the transport direction and speed of sediments, promoting the deposition of sediments within or at the edges of the obstacles, thus creating diverse sedimentary forms and distribution patterns (Kiswaka et al., 2024; Larsen et al., 2023).

During the deposition of the Bottom Sandstone Member, faulting and tectonic activity influenced the Formation of corresponding depositional and erosional areas in the study region. The WM7 fault zone and its western block experienced significant subsidence and, influenced by the Tethys Sea transgression and an arid climate (Zhang S. et al., 2018; Qin et al., 2023), developed a salt lake-delta depositional system. In contrast, the eastern part of the WM7 fault zone is devoid of the Bottom Sandstone Member and features numerous incised valleys, indicating an erosional area where clastic material was transported by rivers and deposited in the fault zone (Figure 14C). Due to the arid climate, evaporitic rocks also formed in the depositional area. Based on the well correlation profiles, it is observed that the sand body thickness is greater in the graben area, while it is relatively thinner in the syndepositional uplift areas, where evaporitic rocks are also developed (Figure 14A). Therefore, the geomorphological features of the syndepositional fault-graben-slope system exert a strong control on sand body distribution.

By comparing sand body thickness, well-seismic profiles, and paleogeography, it was found that due to the fault dip towards the center at both ends of the WM7 fault zone, a graben is formed (Figure 14B). As a result, the accommodation space is larger in the central part of the fault zone, with sand bodies mainly developed in the eastern and central parts of the graben (Figure 14C). The western part of the graben area belongs to the upthrown block of the fault, where the accommodation space is relatively small. Additionally, the fault dip is opposite to the dip of the slope and the direction of the sediment source, which hinders the transportation of sand

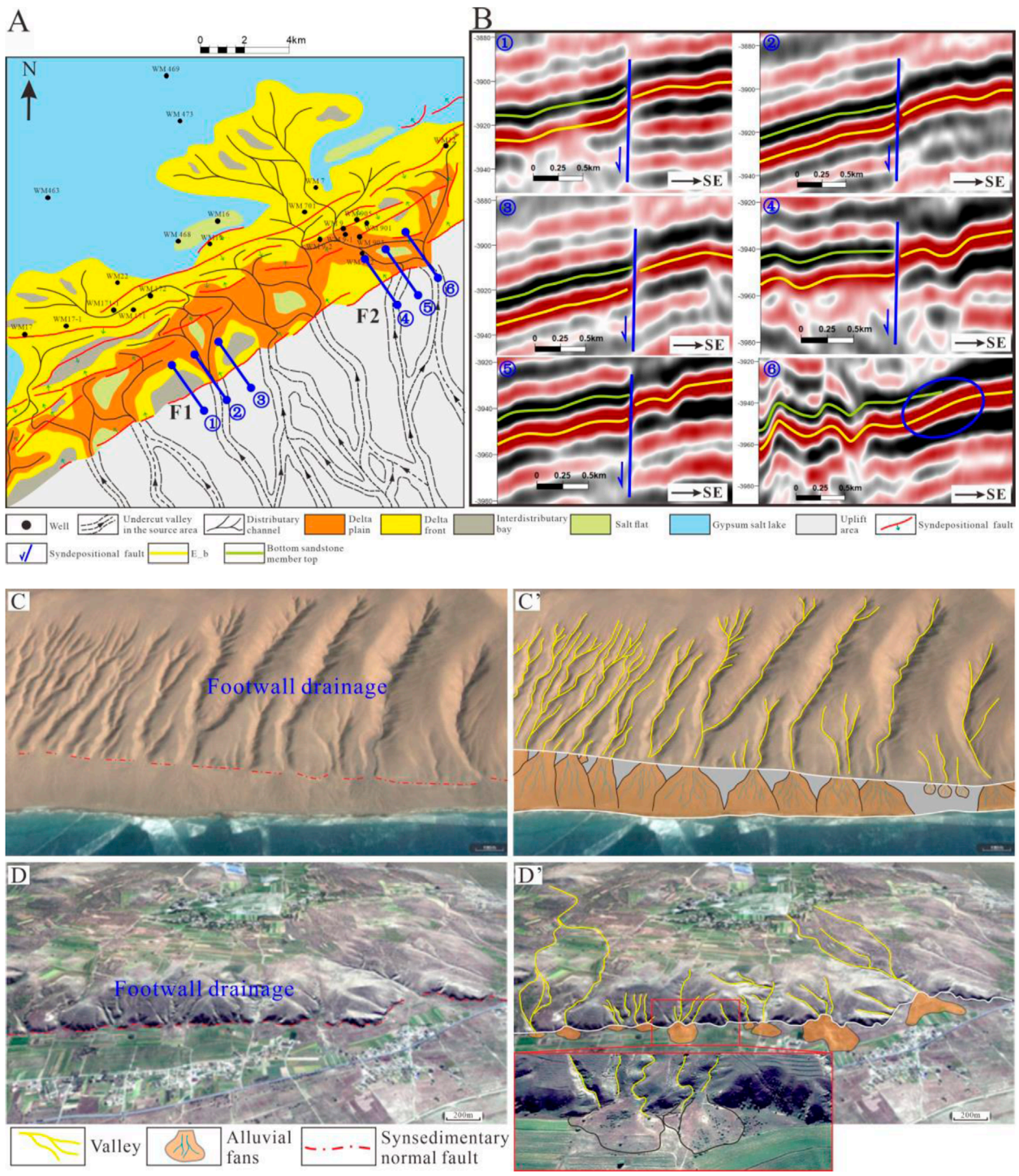

FIGURE 13
Correspondence between fault development characteristics and valleys **(A)** Sedimentary facies of the Bottom Sandstone Member and distribution map of the syndepositional fault in the WM7 fault zone **(B)** Development locations of valleys in the easternmost part of the WM7 fault zone and syndepositional fault characteristics at adjacent locations, with profile positions shown in **(A)**; **(C, D)** Satellite images showing the control of syndepositional faults on valley development **(C)** Syndepositional faults and incised valleys in the northern part of Zhannaicuo Lake, Nima County, Tibet, China **(D)** Syndepositional faults and incised valleys in the southeastern part of Daihai, Inner Mongolia, China. The satellite image in the lower left corner of Figure 13D' is an enlargement of the red box. **(C')** and **(D')** are simplified annotations of **(C, D)**

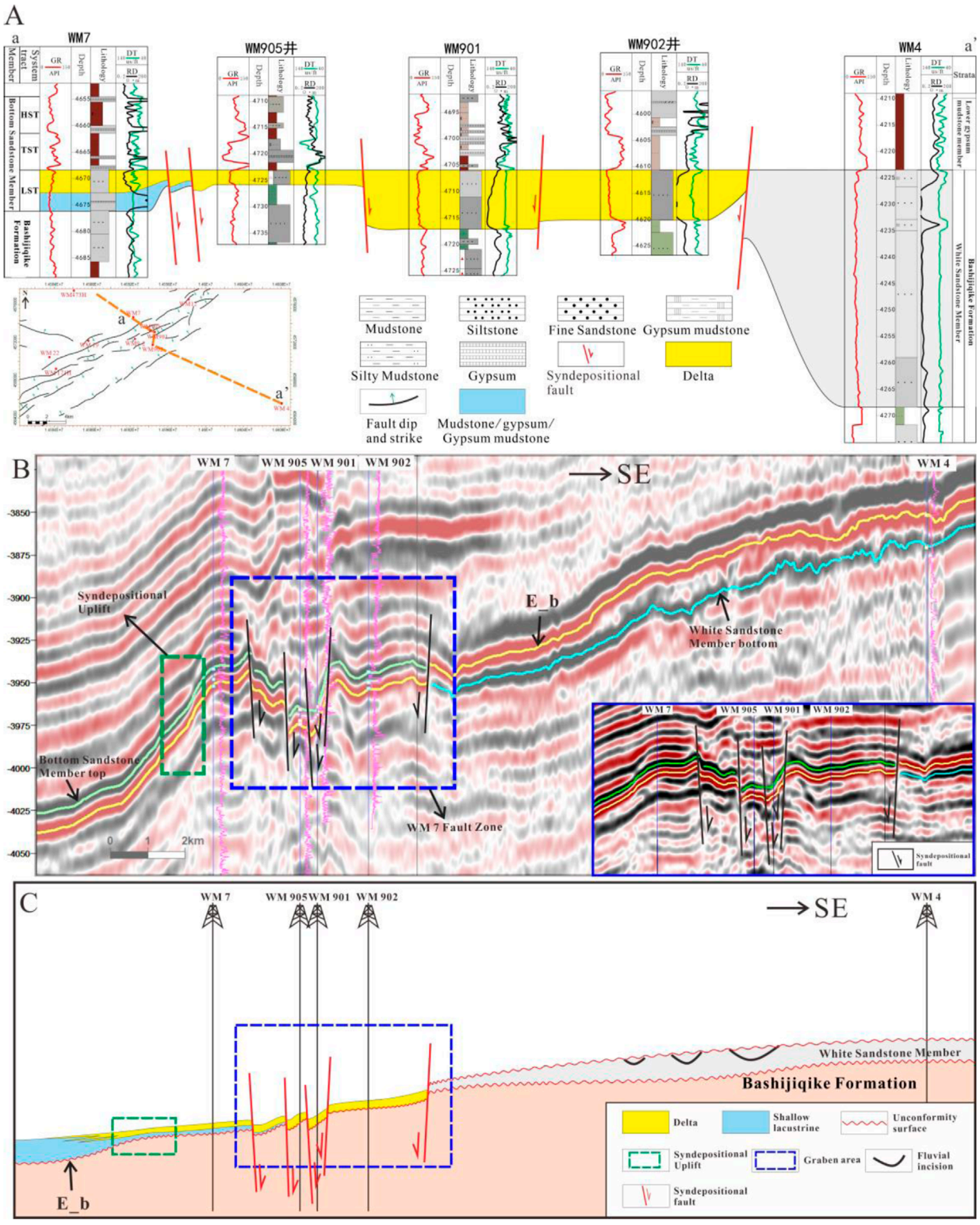

FIGURE 14
Well correlation profiles and seismic profiles along the vertical fault zone direction **(A)** Well correlation profile along wellbores WM7 and WM4, where the Bottom Sandstone Member is only developed in the fault zone and its western block, with relatively thicker sand bodies within the fault zone **(B)** Seismic profile along wellbores WM7-WM4, with an enlarged view of the WM7 fault zone shown in the blue box in the lower right corner. The WM7 fault zone is a large graben, and the strata thickness in the green dashed box is noticeably thinned, indicating the development of a syndepositional uplift **(C)** Sketch diagram created from **(A, B)** showing that the sand bodies primarily developed within the graben. **(B)** represents the present-day structural profile. The elevation of the White Sandstone Member relative to the Bottom Sandstone Member was not as high during the deposition of the Bottom Sandstone Member as it is shown in the current structure. Therefore, in **(C)**, the elevation of the White Sandstone Member relative to the Bottom Sandstone Member has been lowered vertically.

bodies. Influenced by the graben, clastic material is preferentially filled in the central and eastern parts of the graben. The western part of the graben, during the early stage of the Bottom Sandstone Member, had not yet accepted a large supply of clastic material, and the base is developed with mudstone, gypsum, or gypsum-rich mudstone (Figure 14C).

The syndepositional uplift is located to the west of the fault zone (Figure 14C), and it controls the flow direction of the distributary channels. Due to the higher elevation of the syndepositional uplift, the flow velocity of the distributary channels decreases to the east of the uplift, restricting the further progradation of the delta. The sand bodies are mainly concentrated on the eastern side of the uplift (Figure 11D). When the flow velocity of the distributary channels is relatively high, deflection occurs. At locations with a relatively small uplift amplitude, the distributary channels can bypass the syndepositional uplift and continue to deposit forward, forming a fan-shaped body (Figure 11D, the delta to the northwest of wellbore WM7). On the other hand, at the top of the uplift, the accommodation space is relatively small, terrestrial supply is weak, and salinity is high. Under arid conditions, evaporites are likely to form, such as the thick gypsum developed at wellbore WM16 located at the syndepositional uplift (Figure 11D). As a natural barrier, the syndepositional uplift restricts the delta's progradation toward the saline lake, thereby influencing the deposition extent of evaporites.

Inside the graben, the sand body thickness also exhibits variations due to the influence of syndepositional fault assemblages. Previous studies have summarized the control of syndepositional faults on distributary channels by analyzing the relationship between the flow direction of the distributary channels and the dip of the faults. They concluded that distributary channels tend to pass through areas with weaker syntectonic fault activity and are deflected or restricted in areas with stronger fault activity, thereby controlling the development features of the delta (Mulrooney et al., 2018; Dou et al., 2020a). The development of contemporaneous faults also alters the distribution characteristics of the accommodation space and affects the sedimentary filling patterns of the basin (Larsen et al., 2023; Dou et al., 2020b). Building upon this, the present study further summarizes the control of fault assemblage styles on distributary channels and establishes a corresponding sedimentary model (Figure 15).

The WM7 fault zone mainly develops three fault assemblage styles: wall-corner style, domino-style, and graben-horst (Figure 9). For the wall-corner style assemblage, the topography near the fault is relatively elevated. When the flow direction of the distributary channels aligns with the dip of the fault (Figure 15A, F2), the distributary channels will preferentially pass through the fault's transfer zone on the upthrown block, and then deflect toward the direction of the larger fault displacement on the downthrown block. However, the main flow area of the river is located at a certain distance from the fault plane. When the flow direction of the distributary channels is opposite to the dip of the fault (Figure 15A, F1), the distributary channels will bypass the syndepositional fault, pass through areas with low growth indices, and continue to flow downstream. Due to the relatively elevated topography near the wall-corner style syndepositional fault assemblage, the supply of clastic material is relatively limited, leading to the development of interdistributary bays. During low-flow periods, the continuous evaporation of salt lakes resulted in the Formation of salt flats or salt pans.

In the domino-style fault assemblage, due to the opposite dip of the strata and the fault, the topography near the fault on the upthrown block is relatively elevated, resulting in a smaller accommodation space, which is not conducive to the accumulation of sand bodies. This area is dominated by the development of distributary bays and salt flats (Figure 15B). When the flow direction of the distributary channels aligns with the dip of the fault, the channels on the upthrown block preferentially passed through areas of weaker fault activity and the fault transfer zone. Then, they deflected towards areas of stronger fault activity on the downthrown block. The main flow area of the river is relatively close to the fault plane (Figure 15B, F1~F4). When the flow direction of the distributary channels is opposite to the dip of the fault, the channels will preferentially converge in areas of higher fault activity on the downthrown block. Channels with lower flow rates are restricted, while those with higher flow rates and stronger hydrodynamics will preferentially pass through regions with relatively weaker fault activity and continue to extend forward. However, their hydrodynamics will significantly decrease (Figure 15B, F5~F8).

In the graben-horst fault assemblage, the channels will preferentially converge in areas with higher fault activity within the graben, and then occur passive deflection, with the channels being restricted. When the hydrodynamics are strong, the channels will bypass the horst and continue to extend forward. Sand bodies primarily accumulate within the graben (Figure 15C, F1~F3). Due to the limited accommodation space in the horst region, the supply of clastic material is relatively weak, leading to the Formation of distributary bays, salt flats, or salt pans.

Based on the control of sand bodies by syndepositional faults, and combining sedimentary facies and geomorphological characteristics, a syndepositional fault-graben-slope sand control model has been established (Figure 15D). When the river flows from the erosion zone into the graben, it converges in areas of relatively weaker fault activity on the upthrown block, as the flow direction aligns with the dip of the fault. A delta forms within the graben, and under the influence of the complex syndepositional fault assemblages within the graben, the distributary channels undergo passive deflection. During the continuous progradation of the delta, the hydrodynamics gradually weaken due to the blocking effect of syndepositional faults and synsedimentary uplifts. Only a few distributary channels with stronger hydrodynamics can bypass the fault zone and continue to deposit in areas with lower synsedimentary uplift amplitudes. However, the sand body thickness is relatively thin, and the sand body thickness in wells outside the graben is generally less than 2 m. Due to the arid climate in the study area, the salt lake continuously evaporates. Under the influence of syndepositional fault assemblages, salt pans/salt flats are more likely to form in areas with higher topography and weaker clastic material supply, such as the corners of wall-corner style fault assemblages and the horsts in graben-horst fault assemblages. During flood periods, the distributary channels will erode the previously formed evaporites and transport them to other locations, forming mixed deposits (Wang et al., 2023).

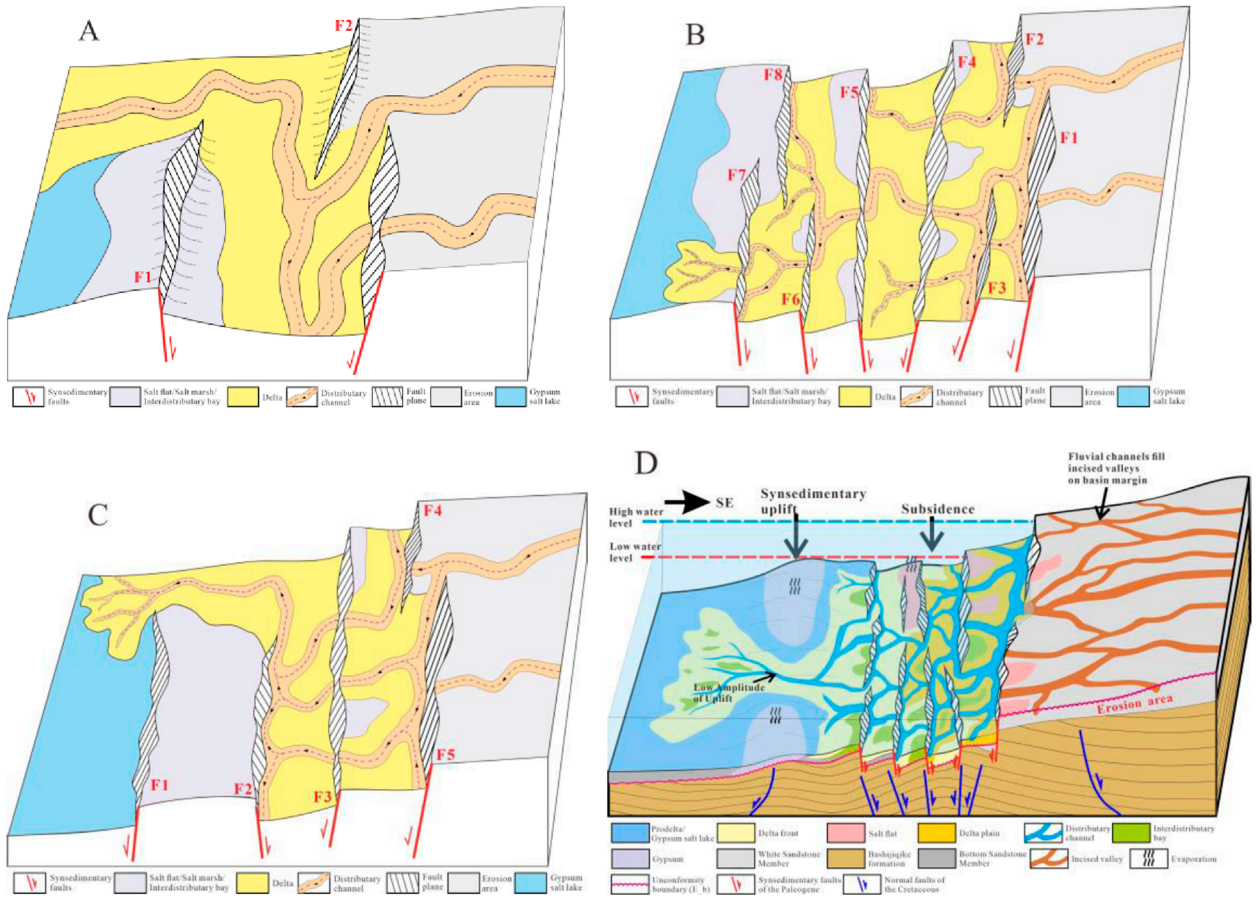

FIGURE 15
Control of different geomorphological units formed by syndepositional faults on sand bodies **(A)** Sand control model of wall-corner style fault assemblage (F1-F2) **(B)** Sand control model of domino-style fault assemblage (F1-F3, F5-F8) **(C)** Sand control model of graben-horst fault assemblage (F1-F2) **(D)** Syndepositional fault-graben-slope sand control model. The erosion zone mainly develops incised valleys, and the river transports clastic material to the WM7 fault zone for deposition. Within the graben, influenced by the syndepositional fault assemblage, the distributary channels undergo passive deflection, with sand bodies primarily deposited in the central and eastern parts of the graben. Under the control of fault assemblages and synsedimentary uplifts, evaporite deposits develop in areas with higher underwater topography.

6 Conclusion

This study, based on 3D seismic data, logging curves, and core descriptions, investigates the depositional environment and the controlling mechanism of sand body accumulation in the Bottom Sandstone Member of the WM7 fault zone. It analyzes the control of paleogeomorphic units formed by small-scale syndepositional normal fault combinations on sand bodies deposition.

(1) The Tabei Uplift underwent complex tectonic movements during the Late Cretaceous to Paleogene periods. During the deposition of the Bottom Sandstone Member, a salt lake-delta depositional system was formed in the study area due to the transgression of the Tethys Ocean and the continuing aridity of the climate.

(2) The eastern part of the WM7 fault zone does not develop the Bottom Sandstone Member, while the fault zone and its western part do. Therefore, during deposition of the Bottom Sandstone Member, the fault zone and its western area served as the depositional area, while the eastern White Sandstone Member was exposed to the surface, undergoing erosion and developing incised valleys that transported clastic material basinward.

(3) Through seismic interpretation and well-seismic profile analysis, it is concluded that during the deposition of the Bottom Sandstone Member, influenced by the 'basement structural weakness zone,' differential subsidence occurred, resulting in the Formation of a large graben in the WM7 fault zone, where numerous small-scale syndepositional faults developed, controlling the distribution of the sand bodies.

(4) The control of the fault zone on sand bodies is mainly manifested in two aspects. Firstly, in the incised valleys of the denuded area, rivers converge in regions with relatively weak fault activity, and clastic rock deposits are formed on the downthrown block. Secondly, the combined patterns of syndepositional faults within the graben cause passive deflection of distributary channels, controlling the aggregation patterns of sand bodies. There are mainly three micro-fault combination patterns: wall-corner style, domino-style, and graben-horst fault assemblages.

Data availability statement

The original contributions presented in the study are included in the article/supplementary material, further inquiries can be directed to the corresponding author.

Author contributions

GX: Conceptualization, Writing–original draft, Writing–review and editing. DL: Formal Analysis, Methodology, Writing–review and editing. HW: Funding acquisition, Project administration, Writing–review and editing. SQ: Writing–review and editing. YZ: Formal Analysis, Validation, Writing–review and editing. LB: Resources, Software, Writing–review and editing. HQ: Investigation, Methodology, Software, Writing–review and editing. JJ: Data curation, Visualization, Writing–review and editing. HY: Funding acquisition, Resources, Writing–review and editing. YJ: Validation, Writing–review and editing. ZL: Software, Validation, Writing–review and editing.

Funding

The author(s) declare that financial support was received for the research and/or publication of this article. This research is supported by the National Natural Science Foundation of China (Grant No. 42202177).

Conflict of interest

Authors SQ, YZ, LB, HQ, and YJ were employed by Tarim Oilfield Company, CNPC.

The remaining authors declare that the research was conducted in the absence of any commercial or financial relationships that could be construed as a potential conflict of interest.

Generative AI statement

The author(s) declare that no Generative AI was used in the creation of this manuscript.

Publisher's note

All claims expressed in this article are solely those of the authors and do not necessarily represent those of their affiliated organizations, or those of the publisher, the editors and the reviewers. Any product that may be evaluated in this article, or claim that may be made by its manufacturer, is not guaranteed or endorsed by the publisher.

References

Allen, J. R. L. (1965). A review of the origin and characteristies of recent alluvial sediments. *Sedimentology* 5 (2), 89–191. doi:10.1111/j.1365-3091.1965.tb01561.x

Alonso-Zarza, A. M., Zhao, Z., Song, C. H., Li, J. J., Zhang, J., Martín-Pérez, A., et al. (2009). Mudflat/distal fan and shallow lake sedimentation (upper Vallesian–Turolian) in the Tianshui Basin, Central China: evidence against the late Miocene eolian loess. *Sediment. Geol.* 222 (1–2), 42–51. doi:10.1016/j.sedgeo.2009.03.010

An, H. T., Li, H. Y., Wang, J. Z., and Du, X. F. (2009). Tectonic evolution and lts controlling on oil and gas accumulation in the northern Tarim Basin. *Geotect. Metallogenia* 33, 142–147. doi:10.16539/j.ddgzyckx.2009.01.019

Arregui, M. G., and Rodríguez, E. (2022). Sedimentological and ichnological signatures from a fluvial-dominated delta in subsurface: lajas Formation, middle Jurassic, Neuquén basin, Argentina. *Lajsba* 29, 97–120.

Benison, K. C., and Goldstein, R. H. (2008). Evaporites and siliciclastics of the Permian Nippewalla Group of Kansas, USA: a case for non-marine deposition in saline lakes and saline pans. *Sedimentology* 48 (1), 165–188. doi:10.1046/j.1365-3091.2001.00362.x

Boyd, R., Dalrymple, R. W., and Zaitlin, B. A. (1994). *Incised-valley systems: origin and sedimentary sequences* Tulsa: SEPM (Society for Sedimentary Geology). doi:10.2110/pec.94.12

Boyd, R., Dalrymple, R. W., and Zaitlin, B. A. (2006). Estuarine and incised-valley facies models, facies models revisited doi:10.2110/pec.06.84.0171

Brian, G. J., and Brian, R. R. (1983). Massive sandstone facies in the Hawkesbury Sandstone, a Triassic fluvial deposit near Sydney, Australia. *J. Sediment. Res.* 53 (4), 1249–1259. doi:10.1306/212F8355-2B24-11D7-8648000102C1865D

Cai, Q. S., Hu, M. Y., Liu, Y. N., Kane, O. I., Deng, Q. J., Hu, Z. G., et al. (2022). Sedimentary characteristics and implications for hydrocarbon exploration in a retrograding shallow-water delta: an example from the fourth Member of the Cretaceous Quantou Formation in the Sanzhao depression, Songliao Basin, NE China. *Petroleum Sci.* 19, 929–948. doi:10.1016/j.petsci.2022.01.018

Cao, Z., Li, P., and Wang, R. (2022). Sequence architecture, slope-break development and geological significance during the P–T transition in the Mahu Sag, Junggar Basin, China. *J. Nat. Gas Geoscience* 7, 237–248. doi:10.1016/j.jnggs.2022.08.001

Cappelle, M. V., Ravnås, R., Hampson, G. J., and Johnson, H. D. (2017). Depositional evolution of a progradational to aggradational, mixed-influenced deltaic succession: Jurassic Tofte and Ile Formations, southern Halten Terrace, offshore Norway. *Mar. Petroleum Geol.* 80, 1–22. doi:10.1016/j.marpetgeo.2016.11.013

Chavanidis, K., Harishidayat, D., Stampolidis, A., Tsokas, G. N., Salem, A., and Soupios, P. (2024). An integrated workflow for characterizing gas potential: axios-Thermaikos basin (Greece). *Acta Geophys.*, 1–22. doi:10.3997/2214-4609.202330008

Chen, C., Cheng, X., Lin, X., Li, F., Tian, H., Qu, M., et al. (2024). Modeling of the Cenozoic subsidence of northern Tarim Basin using elastic plate numerical model: implications for uplift of South Tian Shan. *Earth Sci. Front.* 31, 340–353. doi:10.13745/j.esf.sf.2023.9.43

Chen, H., Li, J., and Zhao, X. (2009). The structural styles of different structural layers in the western part of north tarim uplift and their genetic mechanisms. *Geol. J. China Univ.* 15, 529–536. doi:10.3969/j.issn.1006-7493.2009.04.012

Chen, H., Yang, S., and Dong, C. (1998). Confirmation of permian intermediate-acid igneousrock zone and a new understanding of tectonic evolutionin the northern part of the tarim basin. *Acta Mineral. Sin.* 18, 370–376. doi:10.16461/j.cnki.1000-4734.1998.03.017

Chen, L., Lin, C., Li, H., and Xiang, S. (2017). Sedimentary characteristics of the lower sandstone part of Kumugeliemu group in the western Tabei uplift. *J. Northeast Petroleum Univ.* 41 (5), 23–32. doi:10.3969/j.issn.2095-4107.2017.05.003

Chen, S., Wang, H., Wu, Y., Huang, C., Wang, J., Xiang, X., et al. (2014). Stratigraphic architecture and vertical evolution of various types of structural slope breaks in Paleogene Qikou sag, Bohai Bay Basin, Northeastern China. *J. Petroleum Sci. Eng.* 122, 567–584. doi:10.1016/j.petrol.2014.07.003

Cheng, H. Y., Li, J. H., Zhao, X., and Pan, Y. (2010). Seismic interpretation of occurrence of Permian magmatite and its emplacement in Tabei uplift, Tarim basin. *Acta Petrol. Sin.* 26 (1), 283–290.

Dalrymple, R. W. (2006). Incised valleys in time and space: an introduction to the volume and an examination of the controls on valley Formation and filling, Tulsa: SEPM (Society for Sedimentary Geology). doi:10.2110/pec.06.85.0005

Deng, Q., Hu, M., Wu, Y., Huang, M., Lu, K., Cai, Q., et al. (2025). Lacustrine to deltaic depositional systems: sedimentary evolution and controlling factors of an Upper Cretaceous continental depression and implications for petroleum

exploration. *Mar. Petroleum Geol.* 173, 107234. doi:10.1016/j.marpetgeo.2024.107234

Ding, D., Tang, L., Qian, Y., Liu, W., Lu, X., Cui, K., et al. (1996). Formation and Evolution of the Tarim Basin. Nanjing: Hohai University Press.

Dong, G., He, Y., Leng, C., and Gao, L. (2016). Mechanism of sand body prediction in a continental rift basin by coupling paleogeomorphic elements under the control of base level. *Petroleum Explor. Dev.* 43, 579–590. doi:10.1016/S1876-3804(16)30068-4

Dou, L., Hou, J., Liu, Y., Dr, L., Song, S., and Wang, X. (2020b). Sedimentary infill of shallow water deltaic sand bodies controlled by small-scale syndepositional faults related paleogeomorphology: insights from the paleogene Shahejie Formation in the Dongying depression, Bohai Bay Basin, Eastern China. *Mar. Petroleum Geol.* 118, 104420. doi:10.1016/j.marpetgeo.2020.104420

Dou, L., Hou, J., Zhang, L., Liu, Y., Zhang, L., Wang, X., et al. (2020a). Distribution pattern of deltaic sand bodies controlled by syn-depositional faults in a rift lacustrine basin. *Petroleum Explor. and Dev.* 47, 572–584. doi:10.1016/S1876-3804(20)60074-X

Du, X., Xu, C., Zhu, H., Xie, X., Liu, K., Jiang, Z., et al. (2020). Research advances of mixed siliciclastic and carbonate sediments in continental rift basins. *Earth Sci.* 45, 3509–3526. doi:10.3799/dqkx.2020.251

Du, Y. N., Wu, K. Y., Liu, Y., Li, Y. Y., Cao, Z. C., Cui, Y. W., et al. (2024). Geometry and formation mechanism of tension gashes and their implication on the hydrocarbon accumulation in the deep-seated strata of sedimentary basin: a case from Shunnan area of Tarim Basin. *Petroleum Sci.* 21 (1), 87–99. doi:10.1016/j.petsci.2023.10.021

Feng, Y. (2006). Control of valley and tectonic slope break zone on sand bodies in rift subsidence basin. *Acta Pet. Sin.* 27, 13–16. doi:10.7623/syxb200601003

Fildani, A. (2017). Submarine Canyons: a brief review looking forward. *Geology* 45 (4), 383–384. doi:10.1130/focus042017.1

Harishidayat, D., Niyazi, Y., Stewart, H. A., Al-Shuhail, A., and Jamieson, A. J. (2024). Submarine canyon development controlled by slope failure and oceanographic process interactions. *Sci. Rep.* 14 (1), 18486. doi:10.1038/s41598-024-69536-8

Harishidayat, D., Omosanya, K. O., Johansen, S. E., Eruteya, O. E., and Niyazi, Y. (2018). Morphometric analysis of sediment conduits on a bathymetric high: implications for palaeoenvironment and hydrocarbon prospectivity. *Basin Res.* 30 (5), 1015–1041. doi:10.1111/bre.12291

Harishidayat, D., and Raja, W. R. (2022). Quantitative seismic geomorphology of four different types of the continental slope channel complexes in the canterbury basin, New Zealand. *Appl. Sci.* 12 (9), 4386. doi:10.3390/app12094386

He, Q., Sun, Q., Gao, D., Li, M., Liu, L., Wang, Z., et al. (2024). U–Pb detrital zircon ages from Cretaceous - paleogene white sandstone Member in Western Tabei Uplift (China) as provenance indicators. *Mar. Petroleum Geol.* 160, 106596. doi:10.1016/j.marpetgeo.2023.106596

He, W., Li, J., Qian, X., and Guo, Z. (2001). Mechanism of negative inversion-structuring in north Traim Uplift. *Chin. J. Geol.* 36, 234–240. doi:10.3321/j.issn:0563-5020.2001.02.012

Hou, G., Qu, J., and Zhu, F. (2018). Controlling effect of paleogeomorphology on sedimentary System and sedimentary microfacies: a case study of Cretaceous Qingshuihe Formation in the hinterland of Junggar basin. *J. of China Uni. of Min. Tech.* 47 (05) 1038–1045. doi:10.13247/j.cnki.jcumt.000829

Huang, S., Yang, W., and Lu, Y. (2018). Geological conditions,resource potential and exploration directionof natural gas in Tarim Basin. *Nat. Gas. Geosci.* 29, 1497–1505. doi:10.11764/j.issn.1672-1926.2018.09.012

Jia, C. (1997). *Tectonic characteristics and hydrocarbon Resources of the Tarim Basin in China*. Beijing: Petroleum Industry Press.

Jiang, M., Chen, D., Chang, X., Shu, L., and Wang, F. (2022). Controlling effect of tectonic-paleogeomorphology on deposition in the South of lufeng sag, pearl river mouth basin. *Adv. Geo-Energy Res.* 6, 363–374. doi:10.46690/ager.2022.05.02

Jin, Z., Zhang, Y., and Chen, S. (2005). The tectonic-sedimentary fluctuation process of the Tarim Basin. *Sci. Sin. (Terrae)* 35, 530–539. doi:10.1360/04yd0087

Kiswaka, E. B., Harishidayat, D., Mkinga, O. J., and Saroni, J. J. (2024). Late Cenozoic mass transport deposits in the offshore Tanzania continental margin. *J. Afr. Earth Sci.* 218, 105377. doi:10.1016/j.jafrearsci.2024.105377

Larsen, C., Harishidayat, D., and Omosanya, K. O. L. (2023). Geomorphologic control on the evolution of middle-late miocene submarine channels in the southern taranaki basin, New Zealand. *Mar. Petroleum Geol.* 156, 106447. doi:10.1016/j.marpetgeo.2023.106447

Li, J., Li, M., Fang, X., Wang, Z., Zhang, W., and Yang, Y. (2017). Variation of gypsum morphology along deep core SG-1, western Qaidam Basin (northeastern Tibetan Plateau) and its implication to depositional environments. *Quat. Int.* 430, 71–81. doi:10.1016/j.quaint.2015.12.102

Li, X., Wang, H., Gan, H., Peng, Y., Chen, S., and Zhang, H. (2019). Stratigraphic charactertistic and tectonic control on the paleogene sedimentary evolution of the Baxian Half-graben, Bohai Bay Basin, east China. *J. Petroleum Sci. Eng.* 181, 106145. doi:10.1016/j.petrol.2019.06.009

Li, Y., Zhao, Y., Sun, L., Song, W., Zheng, D., Liu, Y., et al. (2013). Meso-Cenozoic extensional structures in the northern Tarim Basin, NW China. *Int. J. Earth Sci.* 102, 1029–1043. doi:10.1007/s00531-012-0847-3

Lin, C., Pan, Y., and Xiao, J. (2000). Structural slope-break zone: key concept for stratigraphic sequence analysis and petroleum forecasting in fault subsidence basins. *Earth Sci.* 3, 260–266. doi:10.3321/j.issn:1000-2383.2000.03.008

Liu, L., Chen, H., Wang, J., Zhong, Y., Du, X., Gan, X., et al. (2019). Geomorphological evolution and sediment dispersal processes in strike-slip and extensional composite basins: a case study in the Liaodong Bay Depression, Bohai Bay Basin, China. *Mar. Petroleum Geol.* 110, 73–90. doi:10.1016/j.marpetgeo.2019.07.023

Liu, T., Jiang, Z., Jia, H., Wu, X., Yu, J., Zhao, B., et al. (2023). Controlling factors of the gypsum-salt strata differences within two adjacent Eocene sags in the eastern Jiyang Depression, NE China and its hydrocarbon significance. *Geoenergy Sci. Eng.* 231, 212352. doi:10.1016/j.geoen.2023.212352

Luo, S., Tan, X., Chen, L., Li, F., Chen, P., and Xiao, D. (2019). Dense brine refluxing: a new genetic interpretation of widespread anhydrite lumps in the Oligocene–Lower Miocene Asmari Formation of the Zagros foreland basin, NE Iraq. *Mar. Petroleum Geol.* 101, 373–388. doi:10.1016/j.marpetgeo.2018.12.005

Miall, A. D. (1996). *The geology of fluvial deposits*. Berlin: Springer.

Mulrooney, M. J., Rismyhr, B., Yenwongfai, H. D., Leutscher, J., Olaussen, S., and Braathen, A. (2018). Impacts of small-scale faults on continental to coastal plain deposition: evidence from the Realgrunnen Subgroup in the Goliat field, southwest Barents Sea, Norway. *Mar. Petroleum Geol.* 95, 276–302. doi:10.1016/j.marpetgeo.2018.04.023

Nie, Y., Zhu, X., Dong, Y., Yang, K., Ye, L., and Qin, W. (2022). Characterization and research prospect of source-to- sink system elements in continental rift basin. *Geol. Rev.* 68, 1881–1896. doi:10.16509/j.georeview.2022.07.041

Normark, W. R. (1970). Growth patterns of deep sea fans. *AAPG Bull.* 54, 2170–2195. doi:10.1306/5D25CC79-16C1-11D7-8645000102C1865D

Normark, W. R., and Valleys, F. (1978). Channels, and depositional lobes on modern submarine fans: characters for recognition of sandy turbidite environments. *AAPG Bull.* 62, 912–931. doi:10.1306/C1EA4F72-16C9-11D7-8645000102C1865D

Ponce, J. J., Carmona, N., Jait, D., Cevallos, M., and Rojas, C. (2024). Sedimentological and ichnological characterization of delta front mouth bars in a river-dominated delta (Upper Cretaceous) from the La Anita Formation, Austral Basin, Argentina. *Argent. Sedimentol.* 71, 27–53. doi:10.1111/sed.13127

Qin, L., Li, X., Qiu, Z., Li, Z., Xu, S., Li, Y., et al. (2021). Characteristics and formation mechanism of incised valley on the eastern margin of chepaizi uplift, junggar basin. *Geoscience* 35 (3), 832–840. doi:10.19657/j.geoscience.1000-8527.2021.027

Qin, P., Zhong, D., Su, C., Yang, X., Sun, H., Zhang, H., et al. (2023). A unique saline lake sequence in the eastern Tethyan Ocean in responses to the Palaeocene-Eocene thermal maximum: a case study in the Kuqa Depression, Tarim Basin, NW China. *J. Asian Earth Sci.* 250, 105594. doi:10.1016/j.jseaes.2023.105594

Qin, R., Yue, H., Zhou, F., Wu, Q., and Lei, Y. (2020). Characteristics and sedimentary models of sheet sand in shallow lacustrine fluvial-dominated delta front: a case study from lower member of minghuazhen formation in BZ34 area, huanghekou sag. *Acta Sedimentol. Sin.* 38 (2), 429–439. doi:10.1186/s42501-019-0032-8

Shi, Z., Qiu, Z., Dong, D., Zang, C., and He, C. (2017). Controls of paleotectonics,paleoclimate and base level fluctuation on the type and structure of delta front:A case study of the Upper Triassic in the Sichuan Basin, China. *Chin. J. Geol.* 52, 270–284. doi:10.12017/dzkx.2017.018

Shu, J., Henriksen, S., Wang, H., Lu, Y., Ren, J., Cai, D., et al. (2013). Sequence-stratigraphic architectures and sand-body distribution in Cenozoic rifted lacustrine basins, east China. *AAPG Bull.* 97, 1447–1475. doi:10.1306/03041312026

Ta, W., Wang, H., and Jia, X. (2014). Aeolian process-induced hyper-concentrated flow in a desert watershed. *J. Hydrology* 511, 220–228. doi:10.1016/j.jhydrol.2014.01.034

Tang, L., Jin, Z., Zhang, Y., and Lu, K. (1999). Negative inversion structures and geological significance of northern uplift, the Tarim Basin, northwestern China. *Geoscience* 13, 93–98.

Taşgın, C. K., Orhan, H., Türkmen, İ., and Aksoy, E. (2011). Soft-sediment deformation structures in the late Miocene Şelmo Formation around Adıyaman area, Southeastern Turkey. *Sediment. Geol.* 235 (3–4), 277–291. doi:10.1016/j.sedgeo.2010.08.005

Tian, L., Liu, H., Niu, C., Du, X., Lan, X., Chen, D., et al. (2019). Development characteristics and controlling factor analysis of the Neogene Minghuazhen Formation shallow water delta in Huanghekou area, Bohai offshore basin. *J. Palaeogeogr.* 8, 19. doi:10.1186/s42501-019-0032-8

Walker, R. G. (1978). Deep-water sandstone facies and ancient submarine fans: models for exploration for stratigraphic traps. *Bull. AAPG* 62, 932–966. doi:10.1306/C1EA4F77-16C9-11D7-8645000102C1865D

Wang, J., Zhang, D., Yang, S., Li, X., Shi, Y., Cui, J., et al. (2020). Sedimentary characteristics and genesis of the salt lake with the upper member of the Lower Ganchaigou Formation from Yingxi sag, Qaidam basin. *Mar. Petroleum Geol.* 111, 135–155. doi:10.1016/j.marpetgeo.2019.08.006

Wang, K. (2015). Characteristics of the incised valley in the jurassic of the west junggar Basin and its prospect direction, NW China. *Open Access Libr. J.* 2, 1–7. doi:10.4236/oalib.1101745

Wang, Q. H., Xu, Z. P., Zhang, R. H., Yang, H. J., and Yang, X. Z. (2024). New fields, new types of hydrocarbon explorations and their resource potentials in Tarim Basin. *Acta Pet. Sin.* 45, 15–32. doi:10.7623/syxb202401002

Wang, Z. S., Lin, X. B., Fan, J. M., Yang, H. T., Zang, X., and Jia, W. (2023). Occurrence state and deposition of terrestrial gypsum: a case study of the paleogene Suweiyi Formation, yaha area, kuga depression. *Acta Sedimentol. Sin.* 41, 1354–1365. doi:10.14027/j.issn.1000-0550.2023.027

Wei, D., Tan, X., Zhang, D., Kang, Z., Dong, G., Xiao, D., et al. (2022). Occurrence types and genesis of anhydrite from the Ma56 submember of ordovician majiagou formation in central and eastern ordos basin. *J. Palaeogeogr. Chin. Ed.* 24 (2), 226–244. doi:10.7605/gdlxb.2022.02.019

Wei, G., Jia, C., Shi, Y., Lu, H., and Li, Y. (2001). Tectonic characteristics and petroleum accumulation in extensional-shear fault system in mesozoic-cenozoic Formations in the northern area of Tabei Uplift, Tarim. *Acta Pet. Sin.* 22, 19–24. doi:10.7623/syxb200101004

Wei, G., Jia, C., and Yao, H. (1995). The relation of thrust-strike slipstructure and hydrocarbon potential in late of hercynian innorth area of Tarim basin. *Xinjiang Pet. Geol.* 16, 96–101.

Wu, F., Fu, X. F., Zhuo, Q. G., Gui, L. L., Wang, Y., and Lu, H. (2014). Analysis of hydrocarbon accumulation process of Yingmai 7 Structural belt in Kuche Depression based on quantitative fluorescence techniques. *J. Northeast Petroleum Univ.* 38, 32. doi:10.3969/j.issn.2095-4107.2014.04.005

Wu, G., Deng, W., Huang, S., Zheng, D., and Pan, W. (2020a). Tectonic-paleogeographic evolution in the Tarim Basin. *Sci. Geol. Sin.* 55, 305–321. doi:10.12017/dzkx.2020.020

Wu, G. H., Li, Q. M., Xiao, Z. Y., Li, H. H., Zang, L. P., and Zang, X. J. (2009). The evolution characteristics of palaeo-uplifts in tarim Basin and lts exploration directions for oil and gas. *Geotect. Metallogenia* 33, 124–130. doi:10.16539/j.ddgzyckx.2009.01.018

Wu, J., Zhu, C., Yang, G., Zhang, J., Gong, Q., and Song, Y. (2020b). High-resolution sequence stratigraphy characteristics and sedimentary facies evolution of thin sands under high-frequency lake level change:A case study of lower sand Member of Paleogene Kumugeliemu Group in margin of Wensu Uplift-Yingmaili Uplift area. *Petroleum Geol. Recovery Effic.* 27, 38–46. doi:10.13673/j.cnki.cn37-1359/te.2020.06.005

Wu, K., Tan, X., Liu, X., Xue, S., Pang, P., Wu, S., et al. (2024). High-frequency lacustrine lithological and geochemical variations in the eocene qaidam basin: implications for paleoenvironment reconstruction. *Minerals* 14, 79. doi:10.3390/min14010079

Xia, Y., Yang, J., Chen, Y., Lu, S., Wang, M., Yao, Z., et al. (2022). A review of the global polygonal faults: are they playing a big role in fluid migration? *Front. Earth Sci.* 9, 786915. doi:10.3389/feart.2021.786915

Xu, C. (2013). Controlling sand principle of source sink coupling intime and space in continental rift basins: basic idea, conceptual systems and controlling sand models. *China Offshore Oil Gas* 25, 1–11.

Xu, C., Lai, W., Xue, Y., and Cheng, J. (2004). Palaeo-geomorphology analysis for the Paleogene reservoir prediction in Bohai Sea area. *Petroleum Explor. Dev.* 31, 53–56. doi:10.3321/j.issn:1000-0747.2004.05.012

Yang, C., Wu, Q., and Xia, Y. (2000). The origin of Mesozoic-Cenozoic extension-torsional fault system in the north positive element in the Tarim basin, and its role in accumulating oil and gas. *Oil Geophys. Prospect.* 35, 461–468. doi:10.13810/j.cnki.issn.1000-7210.2000.04.008

Yang, H., Jin, Z., Lv, X., Pan, W., and Hu, J. (2007). Basement-involved transpressional structure and the Formation of the bachu uplift, Tarim Basin, northwestern China. *Acta Geol. Sin.* 81, 158–165. doi:10.3321/j.issn:0001-5717.2007.02.003

Yang, S., Chen, H., Ji, D., Li, Z., Dong, C., Jia, C., et al. (2005). Geological process of early to middle permian magmatismin tarim Basin and its geodynamic significance. *Geol. J. China Univ.* 11, 504–511. doi:10.3969/j.issn.1006-7493.2005.04.005

Yang, T., Li, X., Yang, Y., Wen, L., Cao, Z., Wang, X., et al. (2023b). Evolution from shallow-water deltas to fluvial fans in lacustrine basins: a case study from the Middle Jurassic Shaximiao Formation in the central Sichuan Basin, China. *Sedimentology* 70, 1023–1055. doi:10.1111/sed.13163

Yang, Z., Liu, J., Lü, Q., Luo, S., Zhou, X., Li, S., et al. (2023a). Paleogeomorphological restoration and its control on gravity flow sand bodies: a case study of the Chang 73 subMember of the Triassic Yanchang Formation in the Ordos Basin. *Bull. Geol. Sci. Technol.* 42, 146–158. doi:10.19509/j.cnki.dzkq.tb20220023

Yu, H., and Lu, H. (1986). *Principles of structural geology*. Beijing: Geology Press.

Zaman, M. A., Rahman, A., and Haddad, K. (2012). Regional flood frequency analysis in arid regions: a case study for Australia. *J. Hydrology* 475, 74–83. doi:10.1016/j.jhydrol.2012.08.054

Zeng, H. (2011). Seismic sedimentology in China: a review. *Acta Sedimentol. Sin.* 29 (3), 417–426. doi:10.14027/j.cnki.cjxb.2011.03.013

Zeng, H. (2018). What is seismic sedimentology? A tutorial. *Interpretation* 6 (2), SD1–SD12. doi:10.1190/int-2017-0145.1

Zeng, H., Zhu, X., Rukai, Z., and Zhang, Q. (2012). Guidelines for seismic sedimentologic study in non-marine postrift basins. *Petroleum Explor. Dev.* 39 (3), 295–304. doi:10.1016/s1876-3804(12)60045-7

Zhang, J., Xing, F., Wout, K., Zhang, C., Wei, W., Chen, L., et al. (2022). Palaeogeographic reconstructions of the eocene-oligocene Tarim Basin (NW China): sedimentary response to late eocene sea retreat. *Palaeogeogr. Palaeoclimatol. Palaeoecol.* 587, 110796. doi:10.1016/j.palaeo.2021.110796

Zhang, L., Bao, Z. D., Dou, L. X., Zang, D., Mao, D., Song, J., et al. (2018a). Sedimentary characteristics and pattern of distributary channels in shallow water deltaic red bed succession: a case from the Late Cretaceous Yaojia Formation, southern Songliao Basin, NE China. *J. Petroleum Sci. and Eng.* 171, 1171–1190. doi:10.1016/j.petrol.2018.08.006

Zhang, N., Hou, L., He, D., Wang, C., Li, H., and Zhou, C. (2017). Structural characteristics and controlling factors in western Tabei uplift-Kuqa depression area, Tarim Basin. *Geol. Bull. China* 36, 616–623. doi:10.3969/j.issn.1671-2552.2017.04.015

Zhang, S., Hu, X., Han, Z., Li, J., and Garzanti, E. (2018b). Climatic and tectonic controls on Cretaceous-Palaeogene sea-level changes recorded in the Tarim epicontinental sea. *Palaeogeogr. Palaeoclimatol. Palaeoecol.* 501, 92–110. doi:10.1016/j.palaeo.2018.04.008

Zhang, T., Fang, X., Song, C., Appel, E., and Wang, Y. (2014). Cenozoic tectonic deformation and uplift of the South Tian Shan: implications from magnetostratigraphy and balanced cross-section restoration of the Kuqa depression. *Tectonophysics* 628, 172–187. doi:10.1016/j.tecto.2014.04.044

Zhang, Z., Lin, C., Liu, Y., Liu, J., Zhou, H., Li, H., et al. (2021). Lacustrine to fluvial depositional systems: the depositional evolution of an intracontinental depression and controlling factors, Lower Cretaceous, northern Tarim Basin, northwest China. *Mar. Petroleum Geol.* 126, 104904. doi:10.1016/j.marpetgeo.2021.104904

Zhao, J., Mountney, N. P., Liu, C., Qu, H., and Lin, J. (2015). Outcrop architecture of a fluvio-lacustrine succession: upper triassic yanchang formation, ordos basin, China. *Mar. Petroleum Geol.* 68, 394–413. doi:10.1016/j.marpetgeo.2015.09.001

Zhao, X. S., Gao, Z. Y., Feng, J. R., Li, X. P., and Guo, M. L. (2014). Triassic-neogene heavy minerals' assemblages characteristics and basin-orogen tectonic evolution relationship in the Kuqa foreland basin. *Acta Sedimentol. Sin.* 32, 68–77. doi:10.14027/j.cnki.cjxb.2014.01.008

Zhao, Y., Li, Y., Sun, L., Zheng, D., Liu, Y., Wang, D., et al. (2012). Mesozoic-Cenozoic extensional structure in North Uplift of Tarim basin and its genetic discussion. *Acta Petrol. Sin.* 28, 2557–2568. doi:10.0000/36a40e1c9bc841688a5601ed2d365a67

Zhou, Y., Ji, Y., Pigott, J. D., Meng, Q., and Wan, L. (2014). Tectono-stratigraphy of Lower Cretaceous Tanan sub-basin, Tamtsag Basin, Mongolia: sequence architecture, depositional systems and controls on sediment infill. *Mar. Petroleum Geol.* 49, 176–202. doi:10.1016/j.marpetgeo.2013.10.005

Zhu, X. (2000). Sequence stratigraphy. DongYing: China University of Petroleum Press.

Zhu, X. M., Dong, Y. L., Zeng, H. L., Lin, C. Y., and Zhang, X. G. (2020). Research status and thoughts on the development of seismic sedimentology in China. *J. Palaeogeogr.* 22 (3), 397–411. doi:10.7605/gdlxb.2020.03.027

Zhuo, X., Zhang, L., and Chen, X. (2018). The similarity of salt-forming between flume experiment and modern Salt Lake. *Acta Sedimentol. Sin.* 36, 1119–1130. doi:10.14027/j.issn.1000-0550.2018.117